Monthly Notices
of the
ROYAL ASTRONOMICAL SOCIETY

Mon. Not. R. Astron. Soc. **422,** 3339–3355 (2012) doi:10.1111/j.1365-2966.2012.20850.x

Scaling relations of star-forming regions: from kpc-sized clumps to H II regions

Emily Wisnioski,[1⋆] Karl Glazebrook,[1] Chris Blake,[1] Gregory B. Poole,[1] Andrew W. Green,[1,2] Ted Wyder[3] and Chris Martin[3]

[1]*Centre for Astrophysics and Supercomputing, Swinburne University of Technology, PO Box 218, Hawthorn, VIC 3122, Australia*
[2]*Australian Astronomical Observatory, PO Box 296, Epping, NSW 2121, Australia*
[3]*California Institute of Technology, MC 405-47, 1200 East California Boulevard, Pasadena, CA 91125, USA*

Accepted 2012 February 29. Received 2012 February 13; in original form 2011 December 13

ABSTRACT

We present the properties of eight star-forming regions, or 'clumps,' in three galaxies at $z \sim 1.3$ from the WiggleZ Dark Energy Survey, which are resolved with the OH Suppressing InfraRed Imaging Spectrograph (OSIRIS) integral field spectrograph. Within turbulent discs, $\sigma \sim 90\,\mathrm{km\,s^{-1}}$, clumps are measured with average sizes of 1.5 kpc and average Jeans masses of $4.2 \times 10^9\,\mathrm{M_\odot}$, in total accounting for 40–60 per cent of the stellar mass of the discs. These findings lend observational support to models that predict larger clumps will form as a result of higher disc velocity dispersions driven-up by cosmological gas accretion. As a consequence of the changes in global environment, it may be predicted that star-forming regions at high redshift should not resemble star-forming regions locally. Yet despite the increased sizes and dispersions, clumps and H II regions are found to follow tight scaling relations over the range $z = 0$–2 for Hα size, velocity dispersion, luminosity and mass when comparing >2000 H II regions locally and 30 clumps at $z > 1$ ($\sigma \propto r^{0.42\,\pm0.03}$, $L_{\mathrm{H}\alpha} \propto r^{2.72\,\pm0.04}$, $L_{\mathrm{H}\alpha} \propto \sigma^{4.18\,\pm0.21}$ and $L_{\mathrm{H}\alpha} \propto M_{\mathrm{Jeans}}^{1.24\pm0.05}$). We discuss these results in the context of the existing simulations of clump formation and evolution, with an emphasis on the processes that drive-up the turbulent motions in the interstellar medium. Our results indicate that while the turbulence of discs may have important implications for the size and luminosity of regions which form within them, the same processes govern their formation from high redshift to the current epoch.

Key words: H II regions – galaxies: formation – galaxies: high-redshift – galaxies: kinematics and dynamics – galaxies: star clusters: general.

1 INTRODUCTION

Star-forming galaxies at high redshift are generally clumpy, gas-rich and highly efficient at forming stars (Daddi et al. 2010; Tacconi et al. 2010; Combes et al. 2011). Compared to local star-forming galaxies that contain on average hundreds of H II regions, galaxies in the early Universe are made up of a handful of kiloparsec-sized star-forming 'clumps' (Cowie, Hu & Songaila 1995; van den Bergh et al. 1996). These morphologies cannot be explained by simple resolution effects or an imaging *K*-correction (Dickinson 2001). Artificially redshifting images of local star-forming galaxies with distributions of hundreds of H II regions produce high-redshift images with mostly even light distributions (Elmegreen et al. 2009). Furthermore, clumpy structures have been seen in broad-band images as well as UV emission at high redshift, providing evidence for the build-up of massive star clusters (Förster Schreiber et al. 2011a; Guo et al. 2011).

New kinematic data from integral field spectroscopy (IFS) has supplemented the morphological studies to reveal that the clumps are embedded in massive rotating discs with high gas velocity dispersions of 50–200 $\mathrm{km\,s^{-1}}$ (e.g. van Starkenburg et al. 2008; Swinbank et al. 2009; Förster Schreiber et al. 2009; Jones et al. 2010; Genzel et al. 2011; Wisnioski et al. 2011, hereafter Paper I). The clumps are found to have comparable velocity dispersions to the global disc dispersion with typical sizes of ∼1 kpc and masses of $\sim 10^8$–$10^{10}\,\mathrm{M_\odot}$ (Elmegreen & Elmegreen 2005; Elmegreen et al. 2009; Förster Schreiber et al. 2011b; Genzel et al. 2011; Guo et al. 2011).

The kinematic observations are in broad agreement with models of unstable disc formation. In these models, motions in the turbulent interstellar medium (ISM) result in high local velocity dispersions that drive up the Jeans mass and Jeans length resulting in massive star-forming regions in gravitationally unstable discs.

⋆E-mail: ewisnios@astro.swin.edu.au

The time-scale of the clumpy phase is predicted to be short, of the order of ∼0.5 Gyr. The interactions of the clumps and high turbulence heat the gas resulting in a thick disc with scale height of ∼1 kpc. The more massive clumps then spiral to the centre of the galaxy due to dynamical friction to create a bulge (Noguchi 1999; Immeli et al. 2004a,b; Bournaud, Elmegreen & Elmegreen 2007; Elmegreen, Bournaud & Elmegreen 2008).

In more recent models the turbulent discs are continuously fed by cold gas accretion which allows multiple episodes of instability. In these simulations, the clumpy phase can have a lifetime of a few Gyr. Individual clumps last for ∼0.5 Gyr if they have high enough star formation rates (SFRs) to survive destruction by stellar feedback (Krumholz & Dekel 2010). Total SFRs are approximately equal to the accretion rate with most of the galactic star formation occurring in the clumps (∼100 $M_\odot$ yr^{-1}; Dekel, Sari & Ceverino 2009; Ceverino, Dekel & Bournaud 2010). The mass of individual kpc-sized clumps, $\sim 10^8$–10^{10} $M_\odot$, is a few per cent of the mass of the disc amounting to a total of 20 per cent of the mass of the disc (Dekel et al. 2009; Krumholz & Dekel 2010; Genel et al. 2012).

However, there is disagreement amongst the models as to how clumps are able to survive long enough to be prevalent in observations. Clumps with supersonic velocity dispersion and high SFRs are expected to expend all their gas within a disc dynamical time (50 Myr; Dekel et al. 2009) unless something supports them from collapse. Turbulence, a natural candidate, is needed to maintain the high local velocity dispersions and thus the large instability scale. However, the restoring force of turbulence is uncertain with possible sources including gravitational motions of clumps within the disc (Dekel et al. 2009; Aumer et al. 2010; Krumholz & Dekel 2010), disc self-gravity (Immeli et al. 2004b; Bournaud et al. 2007; Burkert et al. 2010; Ceverino et al. 2010), radiative feedback (Murray, Quataert & Thompson 2010; Krumholz & Dekel 2010), supernovae (Mac Low & Klessen 2004; Joung & Mac Low 2006) and gas accretion (Förster Schreiber et al. 2006; Genzel et al. 2006; Genel et al. 2010). However, turbulence is not the only mechanism for stabilizing the clumps. If the regions become rotationally bound they may be supported against total free-fall collapse by their rotation (Agertz, Teyssier & Moore 2009; Aumer et al. 2010; Ceverino et al. 2012).

Furthermore, it is unknown how long individual clumps survive and how they reach their end. In the extreme environments expected in unstable gaseous discs, radiation pressure and momentum-driven galactic winds are expected and may be strong enough to disrupt the clumps before they are able to virialize and fall to the centre to form a bulge via dynamical friction (Genel et al. 2012; Murray et al. 2010).

Kinematic measurements of clump motions and turbulence are therefore essential for understanding how high-redshift galaxies form. Measurements of velocity dispersion of clumps have become more available with the advent of IFS and adaptive optics (AO) systems (Swinbank et al. 2009; Jones et al. 2010; Genzel et al. 2011). These can be used to test clump formation models and the driving forces behind their survival by using gas velocity dispersion as a proxy for turbulence.

Recent IFS observations have suggested that high-redshift clumps may form differently from local H II regions as a result of a more turbulent environment with higher star formation efficiencies, and gas densities. Clumps in intrinsically L_* and sub-L_* galaxies at $z > 2$ have been found to be two orders of magnitude more luminous than H II regions at a given radius (Swinbank et al. 2009; Jones et al. 2010), and their clump gas velocity dispersions lie in the range 60–100 km s^{-1}, two to six times greater than local H II regions (Genzel et al. 2011). However, these properties are comparable to those of the largest H II regions locally, commonly called 'giant' H II regions such as 30Doradus and II Zw 40 which have the same offset in star formation from 'normal'-sized H II regions as high-redshift clumps. This offset in luminosity indicates that both classes have higher star formation surface densities than regular H II regions suggesting that the most apt comparison at the different epochs is between clumps and giant H II regions.

In addition to H II regions and giant H II regions, Hα results of high-redshift clumps have also been directly compared to local giant molecular clouds (GMCs; Murray et al. 2010). Some simulations are based on the assumption that giant clumps at high redshift represent single-star-forming molecular clouds (Krumholz & Dekel 2010; Murray et al. 2010). However, only a few clumps have been observed at high redshift from molecular gas by observing the regions in highly lensed galaxies (Swinbank et al. 2010). It remains unclear what are the best analogues of high-redshift clumps at low redshift and whether the clumps form under the same conditions as GMCs or H II regions.

One strategy to compare star-forming regions at high and low redshifts is to look at scaling relations to see if they evolve with the cosmic time. An investigation of this kind is justified by the literature as extensive research has been dedicated to the relationships found between three key properties: luminosity, size and velocity dispersion for giant H II regions and GMCs (e.g. Terlevich & Melnick 1981; Larson 1981; Gallagher & Hunter 1983; Arsenault & Roy 1988; Bastian et al. 2006; Rozas et al. 2006; Monreal-Ibero et al. 2007). The relationships between size, luminosity and velocity dispersion have been greatly debated with proportionalities ranging from $\sigma \propto r^{1.14\ -3.68}$, $L \propto r^{1.92\ -3}$, $L \propto \sigma^{2.6\ -6.6}$ (Fuentes-Masip et al. 2000; Gutiérrez, Beckman & Buenrostro 2011). However, these discussions often suffer from small-number statistics and biased measurements. We will show that by bringing together multiple studies from the literature, measured in a self-consistent way, the spectrum of H II regions form relatively consistent relationships between size, luminosity and velocity dispersion, which can be extended to include high-redshift clumps. The scaling relationships observed have implications for how star-forming regions form in the changing cosmic environment.

In this paper we present properties of eight clumps from three $z \sim 1.3$ galaxies in the WiggleZ survey. These galaxies were selected from Paper I, in which we presented Hα kinematics of 13 star-forming galaxies observed with IFS. In Section 2 we introduce the WiggleZ clumps and a comparison sample at low and high redshift. We address the most reproducible measures of size, luminosity and velocity dispersion for comparison across 12 Gyr ($z = 0$–5) in Section 3 and apply them to the WiggleZ clumps. In Section 4 we quantify disc instabilities and estimate the mass of star-forming regions. In Section 5 we investigate the scaling relations of size, luminosity and velocity dispersion of star-forming regions and their possible theoretical drivers. In Section 6 we use the results of Sections 3–5 to test predictions from models and simulations of clump formation. In Section 7 we summarize the properties of the WiggleZ clumps presented here. A standard Λcold dark matter (ΛCDM) cosmology of $\Omega_m = 0.27$, $\Omega_\Lambda = 0.73$, $h = 0.7$ is adopted throughout this paper. In this cosmology, at redshift $z = 1.3$, 1 arcsec corresponds to 8.6 kpc in physical coordinates.

2 DATA

In this section we present eight new clumps, at $z > 1$, in galaxies selected from the WiggleZ Dark Energy Survey (Drinkwater et al.

Table 1. High-redshift clump samples.

Paper	z	Parent sample	Number of clumps	Number of galaxies	Radius method[a]
This Work	1.28–1.46	WiggleZ	8	3	Core
Jones et al. (2010)	1.68–2.65	lensed	8	4	Isophote
Genzel et al. (2011)	2.18–2.26	SINS	5	3	Core
Förster-Schreiber et al. (2011b)	2.26	SINS	7	1	Photometric
Swinbank et al. (2009)	4.92	lensed	2	1	Isophote

[a]A more detailed description of how regions were measured is detailed in the Appendix.

Table 2. Low-redshift H II region samples.

Paper	Number of galaxies in parent sample	Parent galaxy types	N^a	Radius method	Dispersion method
SINGS (Kennicutt et al. 2003)	7 NGC	Spirals, irregulars	2091	Core	...
Gallagher & Hunter (1983)	7 NGC; Mk 35; Haro 22; A1004+10	Irregulars	30	Core	Echelle
Arsenault & Roy (1988)	26 NGC; 5 IC; 5 HO	Spirals, irregulars, dwarf irregulars	57	Isophotal	Fabry–Perot
Bastian et al. (2006)	NGC 4038/39 (Antennas)	LIRG	4	Isophotal	IFS
Rozas et al. (2006)	10 NGC	Isolated spirals	43	40 per cent isophotal[b]	Echelle
Monreal-Ibero et al. (2007)	5 IRAS	ULIRGs	12	Half-light	IFS

[a]Number of H II regions used in this paper.
[b]A method that measures core light. The size of the 40 per cent isophote is equal to the diameter of the circle containing the same area as 40 per cent of the peak region surface brightness.

2010) and bring together comparison samples of star-forming regions at high and low redshift. For the comparison samples we only consider clump and H II region data from Hα observations for consistency and due to the wealth of data available in the literature. We focus on studies with published Hα fluxes, sizes and velocity dispersions for individual regions. A summary of the comparison data is given in Table 1 (high redshift) and Table 2 (low redshift); and corrections to the distances, sizes and cosmology that we introduce to improve the comparison of different samples are detailed in the Appendix.

2.1 WiggleZ clumps at $z \sim 1.3$

The new clump data presented in this paper are derived from the IFS observations of Hα luminous galaxies at $z \sim 1.3$ first introduced in Paper I. Data were taken with OH Suppressing InfraRed Imaging Spectrograph (OSIRIS; Larkin et al. 2006) with the Keck II Laser guide star AO system (Wizinowich et al. 2006; van Dam et al. 2006). OSIRIS is a lenslet array spectrograph with a 2048 × 2048 Hawaii-2 detector and spectral resolution $R \sim 3600$. All galaxies were observed with the 0.05 arcsec pixel scale. The full width at half-maximum (FWHM) of the tip-tilt stars ranged from one-and-a-half to two pixels, 0.062–0.1 arcsec, with an average Strehl ratio of 30 per cent estimated from the tip-tilt stars.

Of the 13 galaxies presented in Paper I, three galaxies have Hα morphologies with multiple resolved star-forming regions. A summary of the global properties of these galaxies is given in Table 3. From these data we measure individual Hα clumps and their kinematic properties. Clumps are identified solely from 2D Hα emission images. The unsmoothed raw Hα images used throughout this analysis were created from a summation over the spectral dimension within 1σ of the systemic velocity, as determined by a single-Gaussian fit to the integrated spectrum. None of the galaxies has detectable continuum that could contaminate the Hα images. We find eight resolved clumps in total. The identification of clumps and measurement of their properties are discussed in Section 3.

2.2 High-redshift comparison sample

At high redshift the study of clumps suffers from low-number statistics due to the resolution limits of current instrumentation from the ground. The high-redshift comparison sample consists of 22 clumps at $z > 1.6$ as given in Table 1, which are all at higher redshift than the WiggleZ clumps. The data for two regions are taken from Swinbank et al. (2009) for the lensed $z = 4.92$ galaxy Cl1358+62. Eight regions are obtained from the Jones et al. (2010) lensed sample at $z \sim 2$, and 12 regions are taken from the SINS (Förster Schreiber et al. 2011b; Genzel et al. 2011) at $z \sim 2$. We also compare to simulated high-redshift ($z \sim 1.9$–3.0) clumps extracted from five simulated gravitationally unstable discs with baryonic masses of 10^{10} to 2×10^{11} $M_\odot$ at different stages of their lifetime (Ceverino et al. 2012).

2.3 Low-redshift comparison sample

At low redshift we select a sample of extragalactic H II regions and a sample of giant extragalactic H II regions. The difference between 'normal' H II regions and 'giant' H II regions is determined not only by greater size and luminosity but primarily by having supersonic turbulence ($\sigma > c_{\rm sound}$), a property that was later integrated into the definition of giant H II regions (Smith & Weedman 1970; Terlevich & Melnick 1981; Gallagher & Hunter 1983). The sound velocity for H II regions is defined as $c_{\rm H\,II} = \sqrt{k\mu m T_{\rm H\,II}} = 13\,{\rm km\,s^{-1}}$ where k is the Boltzmann constant, μ is the mean molecular weight, m is the mass of hydrogen and $T_{\rm H\,II}$ is the temperature for H II regions ($\sim 10^4$ K; Fuentes-Masip et al. 2000). For the velocity dispersions to be supersonic a mechanism is required to maintain the turbulence, which is expected to dissipate by shocks within a free-fall time, making them interesting objects to study.

Table 3. Global properties of WiggleZ clumpy galaxies.

ID	z	$f^a_{\rm H\alpha}$	$\log[M_*(\rm M_\odot)]$	$\sigma_{\rm mean}$ (km s^{-1})	$\sigma_{\rm net}$ (km s^{-1})	$v_{\rm shear}$ (km s^{-1})	$12+\log(\rm O/H)$	N^b
WK0912_13R	1.2873	48 ± 16.1	10.7 ± 0.2	81.6 ± 27.7	104.3 ± 27.1	130.5 ± 11.0	<8.47	2
WK1002_61S	1.3039	81.5 ± 5.3	10.7 ± 0.7	85.1 ± 20.3	88.4 ± 4.4	71.5 ± 10.7	<8.37	3
WK0909_06R	1.4602	94.9 ± 6.7	11.0 ± 0.2	92.6 ± 27.8	153.3 ± 8.4	160.8 ± 2.4	8.55 ± 0.1	3

[a]Emission-line flux in units of 10^{-17} erg s^{-1} cm^{-2}.
[b]Number of clumps measured in each galaxy.

The comparison data for the normal H II regions are derived from the *Spitzer* Infrared Nearby Galaxies Survey (SINGS; Kennicutt et al. 2003). The size and luminosity of this sample are measured from publicly available *R*-band continuum-subtracted Hα images using the same methods applied to the WiggleZ data as described in Section 3. We identified 2091 regions from a total of seven galaxies. The Extragalactic Distance Database (EDD; Tully et al. 2009) is used for consistent distance indicators for the SINGS galaxies.

The data for giant H II regions are taken from the literature from different parent populations including ultra-luminous infrared galaxies (ULIRGs), dwarf irregulars and isolated spirals (Gallagher & Hunter 1983; Arsenault & Roy 1988; Bastian et al. 2006; Rozas et al. 2006; Monreal-Ibero et al. 2007). Studies that included Hα velocity dispersion were preferentially chosen from the literature for comparison to the high-redshift IFS data. Values are corrected to the distances from the EDD and cosmology defined in Section 1. Corrections to published data that we introduce to improve the comparison of different samples are described in detail in the Appendix.

3 REGION PARAMETERS

To accurately compare the data from the WiggleZ clumps with the two comparison samples the clump properties from each sample should be measured in a consistent way. In this section we investigate the best methods to determine the radius, luminosity, velocity dispersion and metallicity, and apply them to local H II regions in the SINGS galaxies and to $z \sim 1.3$ clumps in the WiggleZ galaxies. We consider the effects of resolution on these measurements and the implications they will have on the scaling relations studied in Section 5. Results are summarized in Table 4.

3.1 Region size

3.1.1 How to measure size: isophote versus profile fitting?

The size of an individual star-forming region is a difficult but important physical property to accurately measure. Subsequent calculations that depend on the size include region luminosity, velocity dispersion, relative velocity and metallicity. Two methods are traditionally employed to measure region size: the isophote method (Sandage & Tammann 1974) and profile fitting, historically called the 'core' method (Kennicutt 1979). In the isophote method, a radius is derived from the area enclosing a total flux greater than a defined fraction of light or surface brightness level. The isophotal regions selected can be any shape with the radius then characterized from the total area assuming circular symmetry. Depending on the isophote level selected, the regions identified can represent either the cores of H II regions or the core and surrounding diffuse nebulae. The standard choice of isophote varies among studies, with some isophotes selected to encompass a certain percentage of flux while others are selected visually. Conversely, the core method, or profile fitting, measures size by fitting a light profile, most commonly a Gaussian, to the surface brightness profile of each region. The core radius primarily measures the ionized central regions of H II regions, above the surrounding diffuse nebulae.

We measure the isophotal and core radii of H II regions in seven galaxies from the SINGS survey (NGC 0024, NGC 0628, NGC 0925, NGC 1566, NGC 3938, NGC 4254 and NGC 7552). The isophote method selects regions in the SINGS galaxies with surface brightness greater than 1×10^{-16} erg s^{-1} cm^{-2} arcsec^{-2}. This isophote was selected for the ability to distinguish between close bright H II regions while still selecting the majority of H II regions in the core, arms and halo of the listed galaxies. Isophotal radii, $r_{\rm iso}$, were calculated from isophote areas assuming circular symmetry.

Table 4. Properties of clumps in WiggleZ galaxies from OSIRIS Hα data cube.

ID	$v^a_{\rm rel}$ (km s^{-1})	$\sigma^b_{\rm net}$ (km s^{-1})	$\rm SFR^b_{H\alpha}$ ($\rm M_\odot$ yr^{-1})	$r_{\rm core}$ (pc)	$r_{\rm iso}$ (pc)	$\log[M_*(\rm M_\odot)]$	$12+\log(\rm O/H)^b$
WK0912_13R	...	88.4 ± 4.4	20.3 ± 6.8	...	...	...	<8.47
Clump-1	55.4 ± 67.4	140.5 ± 66.5	2.80 ± 1.87	1400	1800	10.5	<8.76
Clump-2	-39.5 ± 18.1	52.03 ± 18.1	1.44 ± 0.64	1000	1100	9.5	<8.60
WK1002_61S	...	104.3 ± 27.7	35.6 ± 2.3	...	...	...	<8.37
Clump-1	27.5 ± 6.4	77.65 ± 6.41	8.31 ± 0.89	1600	1800	10.0	<8.42
Clump-2	3.2 ± 11.9	90.74 ± 11.9	2.54 ± 0.43	900	1200	10.0	<8.46
Clump-3	-32.7 ± 22.9	113.5 ± 22.8	4.98 ± 1.32	1700	700	10.4	<8.62
WK0909_06R	...	153.3 ± 8.4	54.8 ± 3.9	...	...	...	8.55 ± 0.10
Clump-1	130.7 ± 7.5	135.6 ± 7.48	6.62 ± 0.49	1200	2100	10.4	8.57 ± 0.10
Clump-2	-45.7 ± 6.2	72.68 ± 6.23	2.13 ± 0.24	800	1500	9.7	8.38 ± 0.29
Clump-3	-88.3 ± 6.4	80.02 ± 6.43	11.3 ± 1.2	3000	1100	10.3	8.44 ± 0.21

[a]Velocity relative to the systematic redshift.
[b]Calculated within $1r_{\rm core}$.

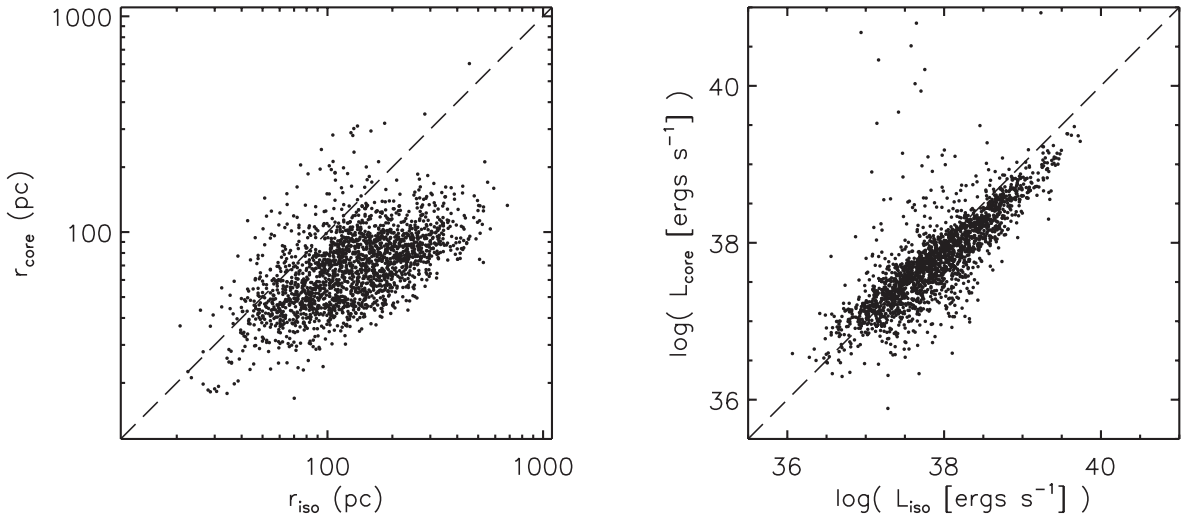

Figure 1. Comparison between radii and luminosity of H II regions measured from the isophote method and the core method in seven galaxies from the SINGS survey (NGC 0024, NGC 0628, NGC 0925, NGC 1566, NGC 3938, NGC 4254 and NGC 7552). We find that the core method measures systematically smaller H II region sizes (left-hand panel) within a small range of sizes but the luminosity measured in both methods (right-hand panel) is consistent. This discrepancy is due to the inclusion of diffuse emission included in some isophotal radii. Although diffuse emission can significantly inflate region sizes, region luminosity is dominated by core emission. Dashed black lines show one-to-one relations.

The core sizes, r_{core}, were measured by fitting a Gaussian to the 1D radial surface brightness profile of each H II region, which provides a good approximation to the data. This profile is chosen because it is the commonly used one in the literature data, and the signal-to-noise ratio (S/N) of the data does not justify a more sophisticated fit.

Fig. 1 shows a comparison between radii measured from the isophote method and the core method for the SINGS galaxies. Whilst the isophote method measures a larger range of sizes (left-hand panel), the luminosity measured in both methods (right-hand panel) is approximately consistent. The discrepancy in measurements arises from how each method accounts for the Hα background, which can affect both size and flux measurements. Small errors, or deviations, in background levels produce large errors in isophotal radii, especially where the diffuse Hα background is bright. Local diffuse tails or haloes of Hα emission around H II regions can also greatly increase the radii causing a significant increase in the scatter of measured sizes. Thus, both image quality and H II region sub-structures can contribute to the discrepancy between sizes from the different measurement methods. Despite the effect of the local background on size, the isophote method yields little to no offset to higher luminosities because the H II region luminosity is dominated by the core. In the core method the total flux of the core is measured above the best-fitting local background level, a free parameter in the Gaussian fit, and therefore the core size measurement contains minimal bias due to the background emission.

The issue of background becomes particularly salient at high redshift. Diffuse H II haloes are either undetected due to their low surface brightness or are smeared together increasing the local background. Therefore, at high redshift the local background could become a significant contaminant, increasing luminosity at a given size as a result of poorer resolution. This would also be an issue when regions are close together, separated by just a few pixels, causing clump light to overlap and combine.

We argue that the core radius is an observationally better determined parameter. The boundary of a core is better defined physically and is less likely to be contaminated by the local diffuse nebular gas. No surface brightness level needs to be assumed or tuned to select H II regions. This method also better serves the comparison of low-redshift and high-redshift data as no flux level or S/N is required for direct comparison. This could be particularly important for high-redshift data in which clumps are only marginally resolved and often separated by only a few pixels. Finally, r_{core} is better justified theoretically because it more closely approximates the central ionized cluster, which will become relevant for future discussions of what drives the relations between radius and other observed parameters (Section 5). A disadvantage of the core method is that it assumes the light profile is a 2D Gaussian and will be subject to systematic error for other distributions.

3.1.2 WiggleZ sizes

Turning now to the WiggleZ sample, we measure the core and isophotal radii of eight clumps from the three galaxies which show multiple resolved clumps: WK0912_13R, WK1002_61S and WK0909_06R. Core radii of the WiggleZ clumps were measured by fitting multiple 2D Gaussians simultaneously to the unsmoothed Hα images. The measurements given in Table 4 represent the 1σ Gaussian widths. In cases where clumps are elliptical, an average radius was calculated. To measure the isophotal radii the isophotes used, $4.5–6.5 \times 10^{-15}$ erg s^{-1} cm^{-2} arcsec^{-2}, were tuned to obtain a reasonable comparison of r_{core} and r_{iso}. Both methods identified the same regions with comparable luminosities. Measurements of r_{core} and r_{iso} are given in Table 4 and the identified clumps are shown in Fig. 2 with the core region sizes overplotted on the Hα images. In the remainder of this paper we use the core radii of the WiggleZ clumps to represent their sizes, $r_{cl} \equiv r_{core}$.

It is likely that the measured clump radius overestimates the actual size of clump-3 in object WK0909_06R. Admittedly, this represents a failing of the core method, such that low S/N diffuse regions are difficult to model with a Gaussian. In object WK0912_13R three clumps can be identified visually in the smoothed image (Fig. 2). However, when fitting 2D Gaussians to the raw images the addition of a third is not justified by the data as this region is unresolved. This region is also not identified at the selected isophote level, which yields similar sizes for clump-1 and clump-2 from the core

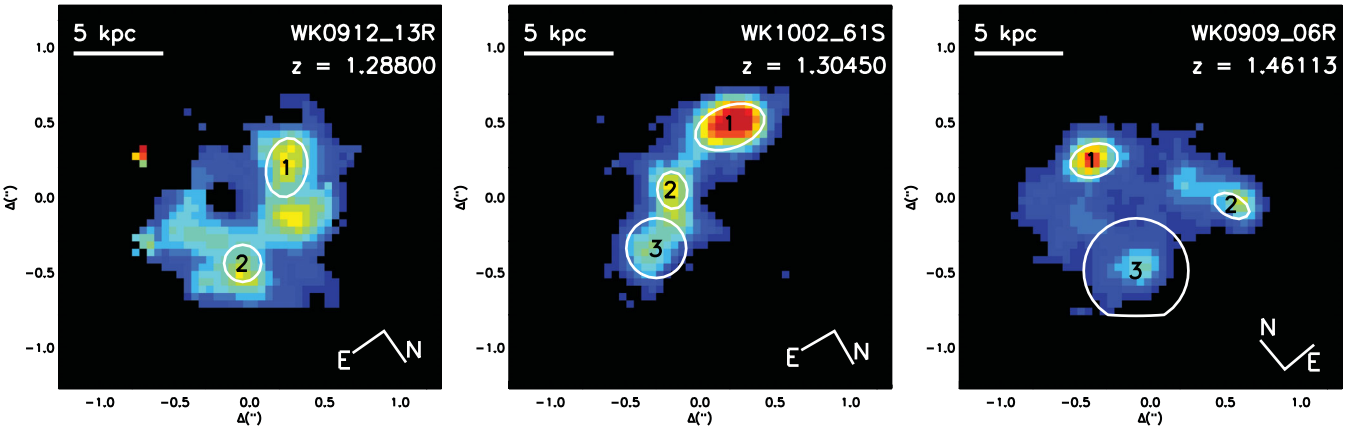

Figure 2. Smoothed Hα flux maps of three clumpy galaxies in the WiggleZ kinematic sample observed with the OSIRIS integral field spectrograph. Clumps identified in Section 3 are shown by the white ellipses. Pixel size corresponds to 0.05 arcsec and the physical orientation is denoted by the compasses in the bottom-right corner. Images are smoothed with a Gaussian kernel with FWHM = 0.15 arcsec.

and isophote methods. Given the uncertainty in measuring clump sizes, arising from degeneracies in the 2D Gaussian fits, resolution effects and systematic error introduced if the regions are not truly Gaussian, we estimate a ∼30 per cent error on the sizes.

3.1.3 Resolution effects

The eight WiggleZ clumps presented here are resolved as are the star-forming regions in the comparison samples. However, it is possible that some WiggleZ clumps are aggregates of unresolved regions since not all clumps are spherical. The resolution of the OSIRIS Hα images studied in the WiggleZ sample is ∼520–840 pc in physical coordinates at $z = 1.3$. Because the WiggleZ clumps are close to being point sources, the Hα luminosity may be underestimated due to the Strehl ratio (∼30 per cent estimated from the tip-tilt stars) as a result of light being spread out by the uncorrected seeing-limited halo.

Despite the regions being resolved, the image resolution may still have implications for the scaling relations investigated in Section 5. Resolution can have the following effects: (1) a core and diffuse emission are smeared together; (2) multiple core regions are smeared together; (3) diffuse emission is smeared to resemble a core and (4) small regions are reduced to noise, with all effects resulting in inflated size and luminosity measurements for the regions observed (Pleuss, Heller & Fricke 2000). Swinbank et al. (2009) investigate the effects of redshifting local galaxy images to $z > 2$ and degrading the resolution on the size and luminosity of regions. They find that only the cores of the highest luminosity H II regions could be observed at high redshift and that lowering the resolution of images blends multiple regions into larger more luminous regions. Both studies find that degrading the resolution results in a steepening of the empirically measured slope between size and luminosity. We readdress these resolution effects in Section 5.

3.2 Region luminosity

The luminosity of each WiggleZ clump is measured from the integrated spectrum created from the spaxels within the 1σ contour of the best Gaussian 2D fit. A Gaussian profile was fitted to the Hα emission in the clump-integrated spectrum with the wavelength, intensity and width as free parameters. Errors were calculated by adding in quadrature an estimation of the sky noise from the variance of the spectrum offset from the emission lines with the Poisson error of the photon counting statistics in the emission lines. Clump SFRs range from 1 to 12 $M_\odot$ yr^{-1} derived from the Hα emission using the Kennicutt (1998) conversion with a Baldry–Glazebrook initial mass function (IMF; Baldry & Glazebrook 2003, hereafter BG03) and are given in Table 4 with SFR densities, $\Sigma_* = \mathrm{SFR}/\pi r_{\mathrm{core}}^2 \sim 0.4$–$2\ M_\odot$ yr^{-1} kpc^{-2}. All the local and high-redshift data have been converted to a BG03 IMF for comparisons in Section 5. A division by 1.82 is required to convert a SFR with a Salpter IMF to a SFR with a BG03 IMF.

For WK0912_13R, WK1002_61S and WK0909_06R the clumps make up 21 per cent, 45 per cent and 37 per cent of the total star formation, respectively, with each clump contributing ∼10 per cent. This is in relative agreement with other IFS studies of emission lines (Genzel et al. 2011) and broad-band studies (Guo et al. 2011; Förster Schreiber et al. 2011b). In galaxies in the *Hubble Deep Field* at $1.5 < z < 2.5$ up to 50 per cent of star formation occurs in clumps with a ∼10 per cent contribution per clump (Guo et al. 2011). In the hydrodynamic cosmological simulations of Agertz et al. (2009) and Ceverino et al. (2010) the giant clumps account for about half of the total star formation at a given time and 20 per cent of the disc mass. For comparison, H II regions in Hα can contribute 30–50 per cent of the gas in local spiral galaxies (Ferguson et al. 1996; Pleuss et al. 2000) and up to 75 per cent with beam-smearing (Pleuss et al. 2000). Thus, the contribution from clump light measured in the WiggleZ sample agrees with high-redshift emission-line samples, well-resolved low-redshift samples and simulated samples.

3.3 Region velocity dispersion

The velocity dispersion of the gas will be dominated by the core region of emission. Although radii measurements are critical for size–luminosity comparisons, variations in the size of the regions have little effect on the integrated velocity dispersion (e.g. Arsenault & Roy 1988). We test this by measuring the velocity dispersion from the integrated spectrum in the clumps of the WiggleZ galaxies within regions of increasing radii. We find that the velocity dispersion does not change by more than one standard deviation when the radius is increased by a factor of 2. As such, although some velocity dispersions in the local sample (Arsenault & Roy 1988) and the high-redshift sample (Swinbank et al. 2009; Jones

et al. 2010) are measured within isophotal radii, the effect on their velocity dispersion measurements should be minimal.

Velocity dispersions, $\sigma_{\rm net}$, for the WiggleZ clumps are derived from the integrated clump spectrum and corrected for instrumental broadening by subtracting the OSIRIS resolution in quadrature and are given in Table 4. We use this measure of velocity dispersion rather than the flux-weighted velocity dispersion, $\sigma_{\rm mean}$ (Law et al. 2007; Green et al. 2010) or other measurements (Davies et al. 2011), for better comparison to the values taken from the literature as it more closely resembles a long-slit observation. Rotation signatures across the clumps are measured to be $\sim$20–80 km s^{-1}, with average $\Delta v/\Delta r_{\rm cl} \sim 15\,{\rm km\,s^{-1}\,kpc^{-1}}$, where Δv is the change in velocity across the clump. This is a small effect in comparison with measured velocity dispersions, as such no correction has been applied. Velocity dispersions of the clumps, uncorrected for beam-smearing, are either consistent with or slightly lower than the total disc dispersions. Total disc dispersions, measured in Paper I, are given in Table 3. Recent simulations show that even with moderate beam-smearing – 0.1 arcsec – the actual observed clump dispersion is highly contaminated by the disc dispersion making it difficult to distinguish between the two signatures (Ceverino et al. 2012). However, the same simulations predict that clump and disc dispersions should be physically comparable in the absence of beam-smearing, minimizing the ramifications for our measurements.

Clumps that have higher mass surface densities than the disc, $\Sigma_{\rm cl} \gg \Sigma_{\rm d}$, could lead to higher dispersions within the clumps due to intense star formation or stellar winds. Large-scale winds can be launched from regions forming stars at $\Sigma_* > 0.1\,{\rm M_\odot\,yr^{-1}\,kpc^{-2}}$ (Heckman et al. 2000) and indeed the WiggleZ clumps measured here have star formation surface densities $\gtrsim$10 times this threshold. If large-scale stellar outflows are driven by the star formation in clumps, inflated velocity dispersions are expected due to an underlying broad wind component (Heckman, Armus & Miley 1990; Genzel et al. 2011). In Fig. 3 we stack the integrated spectrum from all eight WiggleZ clumps at rest wavelength, removing any velocity broadening (Shapiro et al. 2009). The stacked spectrum is fit by two Gaussian components, a narrow peak (FWHM $\sim 170\,{\rm km\,s^{-1}}$), and underlying broad peak (FWHM $\sim 490\,{\rm km\,s^{-1}}$), which has a consistent systemic velocity with relative offset $-24 \pm 30\,{\rm km\,s^{-1}}$. We find that a two-Gaussian fit provides a significant improvement in the value of the chi-squared statistic compared to a one-Gaussian fit, producing a decrease of $\Delta\chi^2 \sim 60$ for the addition of three extra parameters and a reduced χ^2 of 1.07. The broad Gaussian contributes 40 per cent to the total flux. We rule out active galactic nuclei as the driver of the broad Hα component because the clumps are off-centre from the photometric and kinematic centre of the galaxies (Alexander et al. 2010) and no evidence is seen on galactic scale for active galactic nuclei contamination, as discussed in Paper I.

The broad velocity component observed in the stacked WiggleZ clumps has a smaller velocity width and smaller blueshift compared to $z \sim 2$ starbursts galaxies, which may have broad components with up to FWHM $\sim 1500\,{\rm km\,s^{-1}}$ blueshifted by $50\,{\rm km\,s^{-1}}$ (Genzel et al. 2011; Le Tiran et al. 2011b). However, we find that the broad velocity component of the WiggleZ clumps contributes a comparable or larger fraction to the overall flux, equal to 40 per cent. Although a broad component is not detected in the spectra of individual clumps, the presence of a significant broad component in the stack of clump spectra indicates that individual clump velocity dispersion measurements may be overestimated due to contamination from large-scale winds. By comparing to a single-Gaussian fit to the Hα emission of the clump stack, this is estimated to be approximately a 15 per cent effect, or on average $\sim$14 km s^{-1}, comparable to the errors given in Table 4. The possible effect of winds on both clump luminosity and velocity dispersion is reflected in the error bars in the subsequent figures.

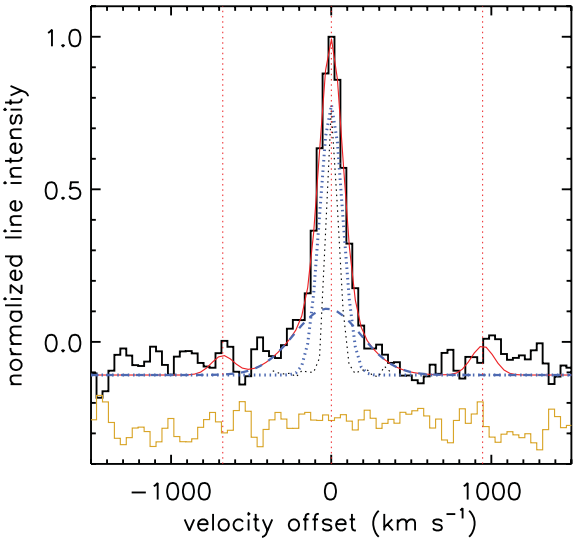

Figure 3. Stack of the integrated Hα spectra from eight WiggleZ clumps corrected for velocity broadening. The red line is the best-fitting model to the Hα and [N II] emission lines composed of two Hα Gaussian components. The blue dotted line is the narrow component with FWHM $= 170\,{\rm km\,s^{-1}}$ and the blue dashed line is the broad component with FWHM $= 490\,{\rm km\,s^{-1}}$ which has a consistent systemic velocity with relative offset $-24 \pm 30\,{\rm km\,s^{-1}}$. The broad component contains 40 per cent of the total flux. The orange line is the residual of the best-fitting model subtracted from the data. The narrow black dotted line at zero velocity shows the instrumental resolution from a stack of sky lines in the observed spectra. Vertical dotted lines show the expected positions of [N II]λ6548, H$\alpha\lambda$6563 and [N II]λ6584.

3.4 Clump metallicity and ages

It has been shown that the scatter in H II region measurements can be partially explained by region metallicity (Terlevich & Melnick 1981; Melnick et al. 1987). Variations in metallicity may also reveal details about the age of clumps, important to their evolution. We calculate clump metallicities for each individual WiggleZ clump and for the clump stack shown in Fig. 3 from the [N II]/Hα ratio following Pettini & Pagel (2004);

$$12 + \log\left(\frac{\rm O}{\rm H}\right) = 8.90 + 0.57 \times \log\left(\frac{\rm [N\,II]}{\rm H\alpha}\right). \quad (1)$$

These values are given in Table 4. For individual WiggleZ clumps a single-Gaussian is fit to the Hα and [N II] emission lines. For the clump stack, the Hα flux used in equation (1) is from the narrow velocity component (shown in Fig. 3 as the dotted blue line). The metallicity of all but the WK0909_06R clumps are upper limits as [N II] in this sample is typically undetected. The stack of eight clumps has a metallicity of $12 + \log({\rm O/H}) = 8.35 \pm 0.31$. All metallicities in individual galaxies are consistent within the errors, which agrees with the simulations of Immeli et al. (2004a) and Bournaud et al. (2008) and implies a common clump evolution history.

4 DISC INSTABILITY

As outlined in Section 1, models predict that clumps form out of gravitational instabilities in gas-rich turbulent discs. The high

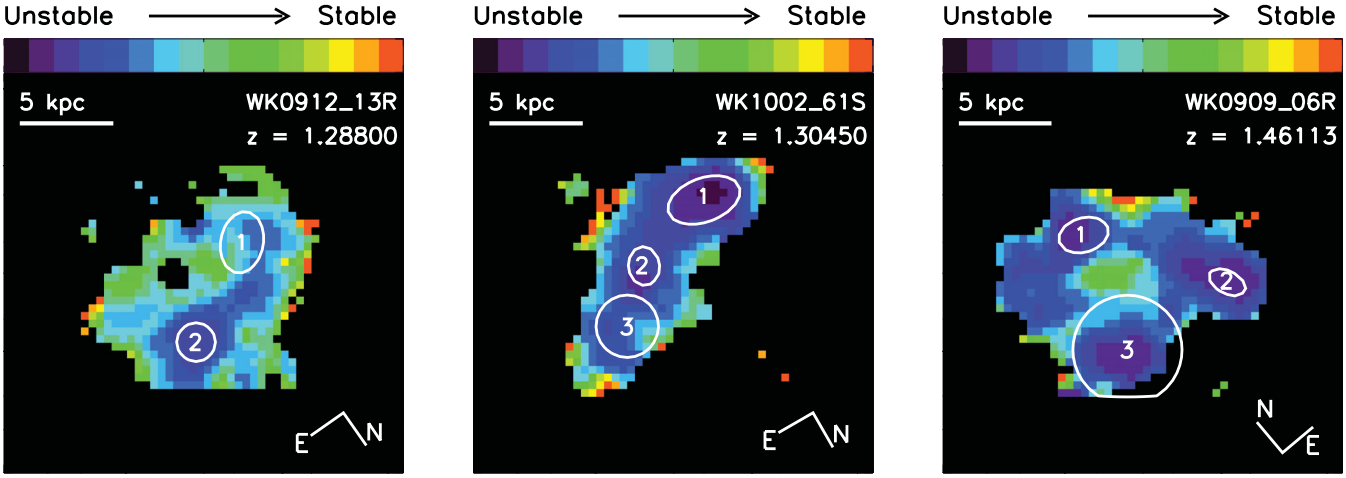

Figure 4. Toomre parameter, $Q_{\rm gas}$ (equation 3), mapped over three clumpy galaxies in the WiggleZ kinematic sample. The calculation of the Toomre parameter assumes the KS law and is uncertain due to the degeneracies of the variables in equation (3). As a result a relative linear scale for $Q_{\rm gas}$ is shown. All three WiggleZ galaxies have areas that are consistent with being in an unstable state ($Q_{\rm gas}<1$) within the errors. Clumps identified in Section 3 are shown by the white ellipses. Likely unstable regions are shown in purple and dark blue. The clumps correlate approximately with Toomre unstable regions.

levels of turbulence are predicted to drive up the expected instability scale in disc galaxies resulting in massive star-forming regions. In this section we characterize the size and mass instability scale of the WiggleZ discs given the high-velocity dispersions measured in Paper I and the previous section. We compare the WiggleZ clumps to the high- and low-redshift samples, which have velocity dispersions ranging from 10 to 100 km s^{-1}. We calculate relative Toomre parameters, shown in Fig. 4, to identify regions of instability where clumps could form.

For star-forming regions to form in gaseous discs, the galaxies must become gravitationally unstable such that $Q < 1$ where Q is the Toomre parameter (Toomre 1964) defined for a pure gas disc as

$$Q_{\rm gas} = \frac{\sigma_{\rm d}\kappa}{\pi {\rm G}\Sigma_{\rm g}}. \quad (2)$$

To test these models of instability we calculate $Q_{\rm gas}$ for the three galaxies hosting clumps in the WiggleZ sample using

$$Q_{\rm gas} = \frac{\sigma}{v_{\rm c}}\frac{a}{f_{\rm g}} \quad (3)$$

as derived from Genzel et al. (2011), where κ is the epicyclic frequency, σ is the local disc gas velocity dispersion, $v_{\rm c}$ is the circular velocity and $\Sigma_{\rm g}$ is the local gas surface density in the disc. The constant a relates the epicyclic and circular frequency in different potentials such that $a = \sqrt{2}$ for a disc with a flat rotation curve (Binney & Tremaine 2008). We estimate the gas fraction, $f_{\rm g}$, from the inverse Kennicutt–Schmidt (KS) law (Schmidt 1959; Kennicutt et al. 2007).

In Paper I, flat disc models were fit to the Hα velocity maps of the WiggleZ galaxies. We obtained estimates for $v_{\rm c}\sin(i)$ rather than $v_{\rm c}$ because the inclination could not be constrained for lack of deep broad-band data and the full extent of the kinematic gas disc is not observed. As a result the actual value of the Toomre parameter across the disc is highly uncertain. A relative Toomre parameter, however, is sufficient to identify the relative stability of the galaxy discs. We note that within the errors of $v_{\rm c}\sin(i)$ for the disc models, $Q_{\rm gas}$ for each galaxy has regions of instability ($Q_{\rm gas} < 1$). In Fig. 4 we show relative Toomre maps for WK0912_13R, WK1001_61S and WK0909_06R. Overlaid on the maps are the clumps identified in Section 3 from the core method. The clumps identified from the Hα maps match to the less stable regions of the discs as expected from the models. These results are in agreement with IFS data at $z \sim 2$ in which Toomre instability correlates with clump location (Genzel et al. 2011). It is expected that low values of $Q_{\rm gas}$ will correlate with regions with high SFRs as the Toomre parameter is proportional to the inverse of star formation as a result of how the gas fraction is calculated. However, significant peaks in local velocity dispersion coincident with the clumps (for example if the clumps are virialized and rotationally supported) could counterbalance the local reduction of $Q_{\rm gas}$ by the star formation. However, this effect is not observed since significantly higher velocity dispersions are not measured in the clumps versus the disc.

When discs are gravitationally unstable, clumps are expected to form under Jeans collapse on a characteristic scale. For the WiggleZ galaxies the expected masses and sizes of the clumps would be limited by the Jeans mass and length, given by

$$\lambda_{\rm J} = \left(\frac{\pi\sigma_{\rm d}^2}{\rho {\rm G}}\right)^{1/2}, \quad (4)$$

and

$$M_{\rm J} = \frac{4\pi}{3}\left(\frac{\lambda_{\rm J}}{2}\right)^3\rho, \quad (5)$$

where $\sigma_{\rm d}$ is the average velocity dispersion in the discs estimated by the velocity dispersions of the clumps and H II regions, and ρ is the density of the disc. By combining equations (4) and (5) and assuming that the measured clump diameter is equal to a Jeans radius, we calculate Jeans masses for the WiggleZ clumps of $M_{\rm J} = 2.2 \times 10^9 - 2.2 \times 10^{10}$ M$_\odot$, which are in agreement with the models (e.g. Krumholz & Dekel 2010). In Fig. 5 we compare the Jeans mass to Hα luminosity for the WiggleZ clumps (red diamonds), the higher-redshift clumps (blue squares and triangles) and the low-redshift giant H II regions (grey points). A tight continuous correlation is seen for all star-forming regions from $M_{\rm J} = 10^6$ to 10^{10} M$_\odot$. The correlation in Fig. 5 combines the three main observables discussed in this paper with scatter characterized by a correlation coefficient of 0.90 and least-squares best fit of $L_{\rm H\alpha} \propto M_{\rm J}^{1.24\pm0.05}$, indicating that the mass closely traces the ionized gas of star-forming regions.

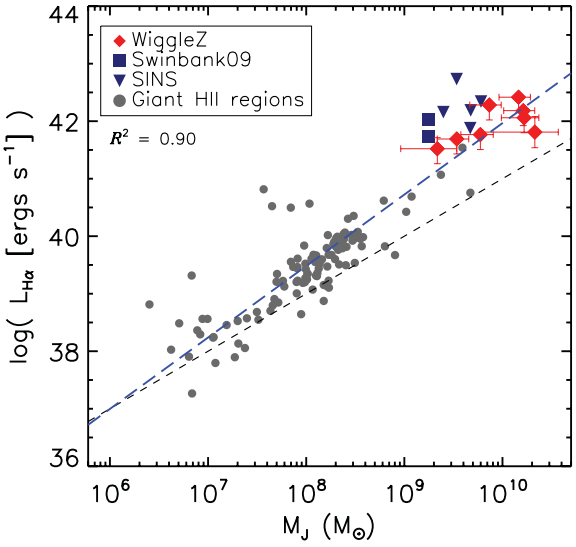

Figure 5. Hα luminosity versus Jeans mass for the WiggleZ clumps (red diamonds), high-redshift comparison sample (blue filled symbols) and low-redshift giant H II region sample (grey points). Hα luminosity and Jeans mass ($M_J = \pi^2\sigma^2 r_{cl}/3G$) show a tight correlation for star-forming regions in local star-forming galaxies (H II regions) to turbulent high-redshift unstable discs (clumps) with sizes of ∼50–5000 pc. The blue dashed line is the least-squares best fit to the data, given by $L_{H\alpha}[\mathrm{erg\,s^{-1}}] = 3 \pm 3 \times 10^{29} M_J[\mathrm{M_\odot}]^{1.24\pm0.05}$. The black dot–dashed line represents $L_{H\alpha} \propto M_J$ arbitrarily normalized for comparison.

5 SCALING RELATIONS OF STAR-FORMING REGIONS

Are the kpc-sized clumps found at high redshift formed out of disc instabilities in a different manner to local H II regions, or are they more massive analogues as suggested by Fig. 5? We show the correlations for measured Hα luminosity, velocity dispersion and size for the WiggleZ clumps, the high-redshift comparison sample, and the low-redshift comparison sample in Fig. 6. We find tight correlations between these properties over 50–5000 pc for H II regions and clumps taken from 11 different studies. Dispersions range between ∼10 and 100 km s^{-1} and Hα luminosities span five orders of magnitude. Assuming equal weighting for all points we use linear least-squares fitting to find the best fit to the relations to be

$$\begin{aligned} \log(\sigma) &= (0.42 \pm 0.03) \times \log(d) + (0.33 \pm 0.09), \\ \log(L_{H\alpha}) &= (2.72 \pm 0.04) \times \log(d) + (31.99 \pm 0.08), \\ \log(L_{H\alpha}) &= (4.18 \pm 0.21) \times \log(\sigma) + (33.61 \pm 0.31), \end{aligned} \quad (6)$$

where $L_{H\alpha}$ is measured in erg s^{-1}, d in pc and the σ in km s^{-1}, with correlation coefficients, R^2, of 0.72, 0.82 and 0.87, respectively. These fits are overplotted as blue dashed lines in Fig. 6. Simulated clumps are included in Fig. 6 (orange points) for comparison to the data, but are not included in the above fits. Below we discuss the scaling relations and their possible drivers.

5.1 Velocity dispersion versus size

We derive the relation between size and velocity dispersion for regions that form out of Jeans collapse in an isothermal disc. The disc scale height, H, for an isothermal disc is given by

$$H \equiv \frac{1}{\rho_0} \int_0^\infty \rho(z)\,\mathrm{d}z, \quad (7)$$

(Spitzer 1942) where ρ_0 is the midplane density value and z is the height above the plane. The scale length has the solution for a purely self-gravitating unmagnetized gas dominated disc

$$H_\infty = \frac{\sigma}{(2\pi G\rho_\infty)^{1/2}} = \frac{\sigma^2}{\pi G \Sigma_g}, \quad (8)$$

where H_∞ and ρ_∞ are the disc scale height and density in this limit with σ defined as the turbulent velocity dispersion. The surface density of the disc is given by $\Sigma_g = 2H_\infty\rho_\infty$. Therefore we obtain an equation for the density such that

$$\rho_\infty = \frac{\pi G \Sigma_g^2}{2\sigma^2}. \quad (9)$$

Combining this with the definition of the Jeans length in equation (4), assuming $\rho = \rho_\infty$, we obtain a threshold length for the regions forming under Jeans collapse in an isothermal disc such that

$$\lambda_J < \frac{\sqrt{2}\sigma_d^2}{G\Sigma_g}. \quad (10)$$

The corresponding mass limit from equation (5) becomes $M_J < \sqrt{2}\pi^2\sigma^4/6G^2\Sigma_g$. To associate this scaling with measured size we adopt the convention of Dekel et al. (2009) which relates the typical clump radius to the Jeans scale as $r_{cl} \simeq \lambda_J/2$. Thus, we define region diameters to be $\simeq \lambda_J$ as plotted in Fig. 6. We fit equation (10) to the first panel in Fig. 6 and obtain a normalization for the gas surface density of $\Sigma_g = 600\ \mathrm{M_\odot\ pc^{-2}}$.

We use the correlation between size and dispersion defined in equation (10) to estimate the gas surface density and test the KS law for individual star-forming regions. We assume that at the time of collapse, star-forming regions should have comparable surface densities and velocity dispersions to the disc in which they formed, and that the mass of the star-forming regions is dominated by gas ($\Sigma_g = \sqrt{2}\sigma_{cl}^2/Gr_{cl}$). This is only an approximation as the regions are not purely molecular. Therefore, it is expected that the gas surface density determined by equation (10) should always be higher than the molecular gas surface density as estimated from the KS law. In Fig. 7 the star formation surface density is plotted against the derived gas surface density for the low- and high-redshift regions. The KS law (Kennicutt et al. 2007) is overplotted by the black dot–dashed line corrected to a BG03 IMF. The derived gas surface density for all regions is indeed greater than expected from the KS law, but is otherwise a reasonable approximation to the true gas surface density. The linear least-squares fit to the data gives a slope of 1.38 ± 0.14 as shown by the blue dashed line and correlation coefficient of 0.66, consistent with the slope of 1.4 predicted by the KS law. We note that the fit degrades at high redshift. This could be due to a selection effect given that we can only observe regions with the highest star formation surface densities.

Using this method we obtain upper limits on the gas surface densities of the order of ∼500–3000 $\mathrm{M_\odot\ pc^{-2}}$ for WiggleZ clumps, which overlap with the star formation surface densities for giant H II regions (∼100–3000 $\mathrm{M_\odot\ pc^{-2}}$), and are comparable to the mean gas surface density for clumps at $z \sim 2$ (Ceverino et al. 2010; Genzel et al. 2011). To emphasize the difference between the local and high-redshift environments in these instances, clumps have been compared to local GMCs which have typical surface densities of ∼60–170 $\mathrm{M_\odot\ pc^{-2}}$ (Blitz et al. 2007; Bolatto et al. 2008; Heyer et al. 2009). However, we argue that clumps are more comparable observationally and physically to H II regions than GMCs as they are observed from their OB stars, which have already formed out of molecular gas.

The size–velocity dispersion relation shows the most scatter in Fig. 6 with correlation coefficient of 0.72. Is this scatter due to measurement errors or an expected spread in region surface density

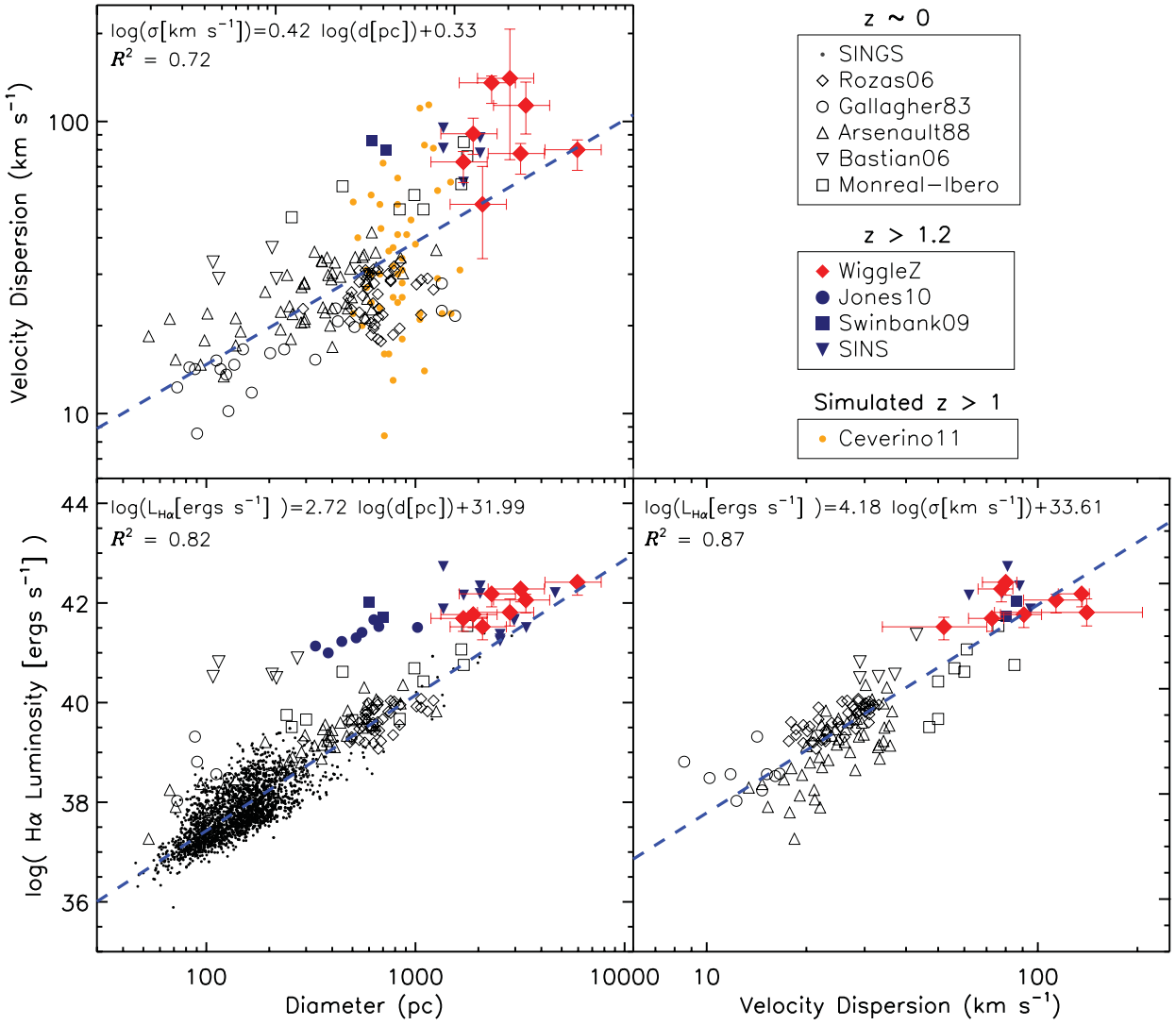

Figure 6. Relations between the Hα luminosity, size and velocity dispersion of H II regions in local star-forming galaxies and clumps in high-redshift galaxies. Clumps from WiggleZ galaxies are represented by the bright red diamonds. High-redshift clumps are shown as filled symbols in blue and taken from Swinbank et al. (2009), Jones et al. (2010), Genzel et al. (2011) and Förster Schreiber et al. (2011b). H II regions from local SINGS galaxies are displayed as black dots, and giant H II regions from local galaxies are shown as open black points and are taken from Gallagher & Hunter (1983), Arsenault & Roy (1988), Bastian et al. (2006), Rozas et al. (2006) and Monreal-Ibero et al. (2007). The blue dashed lines show the least-squares best fits, given in the top-left corner of each panel with correlation coefficients, R^2, given directly below. Simulated clumps at $1.9 < z < 3.0$ from Ceverino et al. (2012) are plotted in orange but have not been included in the fit.

in accordance with the KS law? The scatter in velocity dispersion ranges from ~20–90 km s^{-1} while the average error on the measured velocity dispersion of the WiggleZ clumps is ~20 km s^{-1}. This scaling is expected to show scatter due to measurement errors discussed in Section 3: size is the most uncertain parameter to measure, and the contribution of galactic winds in and around star-forming regions may result in added scatter in the velocity dispersion measurement. However, if regions are expected to follow the KS law (as Fig. 7 tentatively suggests) then from the three order-of magnitude spread measured in Σ_* a range of ~4000 M$_\odot$ pc^{-2} in Σ_g would be expected. This range translates into a spread in velocity dispersion of ~60 km s^{-1} at a given radius, approximately equivalent to the average scatter in Fig. 6 and greater than the typical errors on velocity dispersion of the WiggleZ sample. Thus, if the KS law holds, then the expected variations in the gas surface density can explain the scattered relation between size and dispersion.

The same scaling between size and velocity dispersion, $\sigma \propto r^{1/2}$, can be obtained for virialized objects from the equation of dynamical mass ($M_{\rm dyn} = 5\sigma^2 r_{\rm cl}/{\rm G}$) and assuming a constant surface density such that $\sigma^2 = \pi {\rm G}\Sigma r_{\rm cl}/5$. When this relation is fit to the data in Fig. 6 the best-fitting average mass density for all regions, $\Sigma = 600$ M$_\odot$ pc^{-2}, is equivalent to the surface density derived using the Jeans scaling. From the scatter in Fig. 6 the mass densities for all regions range from 100 to 5000 M$_\odot$ pc^{-2} similar to what is seen in Fig. 7 and discussed above. If regions have virialized then their mass will be better represented by the dynamical mass, which follows the same scaling as the Jeans mass ($M \propto \sigma^2 r/{\rm G}$) determined in Section 4. However, the virial scaling yields masses of a factor of three times greater than their Jeans mass. When the dynamical clump masses are added within their respective discs they approximate ~50–90 per cent of the total stellar mass, compared to the Jeans masses which amount to ~40–60 per cent of the total stellar masses of

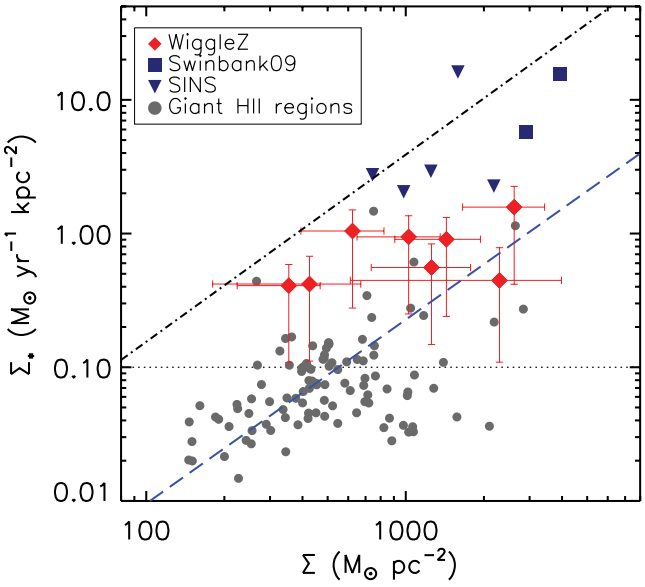

Figure 7. Star formation surface density (Σ_*) versus gas mass surface density (Σ_g; derived from equation 10) for the same data described in Fig. 6 with all giant H II regions now shown by grey points. The black dot–dashed line is the KS law, $\Sigma_* \propto \Sigma_g^{1.4}$ from Kennicutt et al. (2007). The average gas surface density for the WiggleZ clumps, assuming the KS law, derived from the measured Σ_* is $\sim$500 $M_\odot$ pc^{-2} in comparison to what is derived from the Jeans equations for a pure gas disc of $\Sigma_g \sim 1000$ $M_\odot$ pc^{-2}. The blue dashed line is the least-squares fit to the data given by $\Sigma_*[M_\odot\ \mathrm{yr}^{-1}\ \mathrm{kpc}^{-2}] = 2 \times 10^{-5}\Sigma_g[M_\odot\ \mathrm{pc}^{-2}]^{1.37\pm0.14}$. The horizontal line represents the threshold of star formation required to host stellar winds (Heckman et al. 2000). The star formation surface density and KS law are plotted for a Baldry–Glazebrook IMF.

the discs. The Jeans masses are more comparable to the expected masses from individual clumps, and to the total mass contribution of clumps to the whole system, predicted by simulations (Dekel et al. 2009; Krumholz & Dekel 2010; Ceverino et al. 2012). Thus, it seems unlikely that all the observed clumps have virialized and constitute such a large mass fraction of their discs.

We note that the high-redshift clumps, from the WiggleZ and SINS data sets, on average have higher velocity dispersions than predicted by the best-fitting relation described by equation (6). If we assume that the clumps from both samples are contaminated by galactic scale winds, as suggested here and in Genzel et al. (2011), with an average contribution comparable to the result of our stacking analysis in Section 3.3, then the high-redshift dispersions are reduced by a factor of $\sim$0.85 making them more consistent with the scaling relation of equation (6).

5.2 Luminosity versus size

The scaling of Hα luminosity with size of H II regions is well understood if size is represented by the radius of a Strömgren sphere, r_s, the boundary between ionized and neutral hydrogen. The luminosity of an ionization-bound region scales as $L_{H\alpha} \propto r^3$, or more specifically

$$L_{H\alpha} = \frac{4\pi}{3}\frac{{N_H}^2 \alpha_B hc}{\lambda_{H\alpha}} r_s^3, \quad (11)$$

where N_H is the ionized hydrogen number density and α_B is the Case-B recombination coefficient assuming $T_{H\,II} = 10\,000$ K (Osterbrock 1989). We obtain a density of $N_H \sim 500\,\mathrm{cm}^{-3}$ by normalizing the scaling relation to the data and assuming $r_s = r_{cl}$. For comparison, $N_H \sim 100\,\mathrm{cm}^{-3}$ in local ULIRGs (Monreal-Ibero et al. 2007). The residual from subtracting a least-squares fit, fixing $L \propto r^3$, from the data is shown in Fig. 8. However, this is an idealized relation which assumes direct observations of individual Strömgren spheres at a constant number density and temperature. The empirical relation observed in our data yields a slightly shallower slope of 2.72 ± 0.04, which could result from a variety of factors that act alone or in aggregate. Below, we investigate the physical and observational processes that could affect the slope of the relation as well as consider the scalings of GMCs.

If the hydrogen atoms within the cloud can recombine faster than they can be ionized then not all the ionized photons will be absorbed. In this case, the ionization region is said to be density bound, as the observed luminosity is limited by the density of the cloud, and could explain deviations from the scaling relation such that regions are less luminous at a given radius. A detailed discussion of this scenario can be found in Beckman et al. (2000) and the references therein. In this study all regions with $L_{H\alpha} > 10^{38.6}$ erg s^{-1} are predicted to be density bound due to a constant surface density for GMCs from which they form. We note that all of the WiggleZ clumps and the majority of giant H II regions studied here are more luminous than this threshold, which suggests that a shallower slope could be observed as a result. An important consequence of regions being density bound is that escaping photons could be responsible for ionizing the diffuse ISM in the disc.

As discussed in Section 3.1.3, resolution can affect the size–luminosity scaling relation. Beam-smearing results in a steeper slope in size–luminosity space than expected for resolved regions (Pleuss et al. 2000; Swinbank et al. 2009). Therefore, if the Strömgren sphere scaling is the correct theoretical prediction for the empirical relation of size–luminosity, then resolution is not the dominant effect on the slope and may counterbalance other processes that result in a shallower slope (e.g. when regions are density bound). Dust, metallicity and magnetic fields are also likely to reduce the observed ionized radiation at a given size; however a detailed discussion of their effects is beyond the scope of this paper.

If the more appropriate analogues to Hα clumps are GMCs rather than H II regions as suggested in the literature (Murray et al. 2010; Krumholz & Dekel 2010) then a different scaling is expected between luminosity and size. For this case, a molecular tracer of radiation is necessary. The scaling between CO luminosity and size for molecular clouds follows a shallower relation, than expected from Strömgren spheres, of the order of $L \propto r^{5/2}$ (Solomon et al. 1987; Elmegreen 1989). However, although this scaling provides a reasonable fit to the H II region data shown in Fig 8, it assumes a CO luminosity and cannot be tested by our Hα data. We note that a similar relationship, of the order of $L \propto r^3$, has been observed between lensed clumps at $z = 2.3$, GMC cores and young H II regions for L_{260}, a tracer of molecular gas (Swinbank et al. 2010). These results suggest that the underlying physics of the star-forming processes are similar from $z = 2.3$ to the present-day Universe.

Some observations (Swinbank et al. 2009; Jones et al. 2010) of high-redshift clumps show deviations from the empirical luminosity–size relation. In these results the clumps in both a lensed L_* galaxy at $z \sim 5$ and lensed sub-L_* galaxies at $z \sim 2$ are offset by two orders of magnitude in luminosity from local H II regions (blue filled circles and squares in Figs 6 and 8). An interpretation of the observed offset is that these regions, as well as giant H II regions, form due to a starburst mode or due to lower metallicities of high-redshift galaxies. In comparison, there is a half order of magnitude offset in luminosity of the WiggleZ and SINS clumps from the best-fitting relation to all the regions. A fraction of the

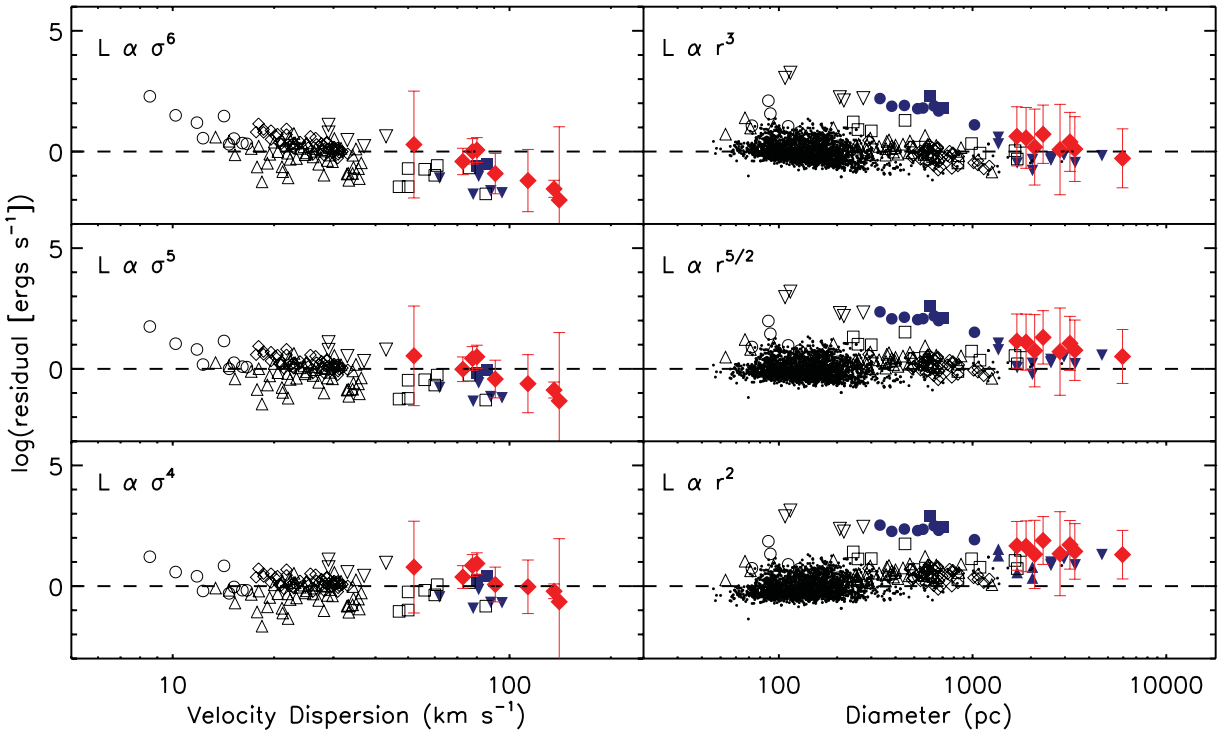

Figure 8. Residual luminosity versus velocity dispersion and diameter from linear least-squares fit assuming the scaling relations between luminosity and velocity dispersion and luminosity and size denoted in the upper-left corner of each panel. Symbols and colours are the same as in Fig. 6. The relations are derived for (top) ionization bound Strömgren spheres that formed from Jeans collapse in an isothermal disc, (middle) GMCs and (bottom) virialized regions. The L–σ relation is best approximated by $L \propto \sigma^4$ and the L–r relation is best approximated by $L \propto r^3$. These scaling relations are discussed in detail in Sections 5.2 and 5.3. The most deviant points in the right-hand panels, offset by two orders of magnitude in luminosity, are from locally LIRG merger of NGC 4038 and NGC 4039 (open inverted triangles), lensed sub-L_* galaxies at $z \sim 2$ (blue closed circles) and an L_* galaxy at $z \sim 5$ (blue closed squares). The offset could be due to a difference in how regions are measured, as both high-redshift studies used the isophote method rather than profile fitting and the determination of sizes in the low-redshift sample is unclear.

offset in the WiggleZ and SINS clumps is likely due to an inflation of the clump luminosities from large-scale winds. The analysis in Section 3.3 suggests that winds can contribute up to 40 per cent of the luminosity of a region. If the luminosity of the WiggleZ and SINS clumps are corrected for this effect the remaining offset is less than half an order of magnitude from the best-fitting relation. While a slight offset in luminosity exists for the WiggleZ clumps, it is small in comparison to the two order of magnitude offset found for the lensed clumps. The remaining offset could be a result of the factors discussed in this section. We find no significant luminosity offset between H II regions and giant H II regions at a given size. Furthermore, we include data from other low-metallicity regions with comparable values and find that they fall on the main relation. Thus, another basis is required to explain the deviation of the lensed regions. One possible explanation for the discrepancy is that the sizes of the regions from the two lensed studies are measured by the isophote method which could overestimate the luminosity for a given region by including surrounding flux of the disc.

5.3 Luminosity versus velocity dispersion

Assuming from our discussion above that H II regions and clumps are idealized Strömgren spheres ($L \propto r^3$), which form out of Jeans collapse in an isothermal disc ($r \propto \sigma^2$), then it is expected for luminosity to scale with dispersion as $L \propto \sigma^6$. This scaling can also be derived from the gas accretion rate as a function of virial velocity and the energy deposition rate due to accretion (Dekel & Birnboim 2008; Le Tiran et al. 2011a). However, as outlined in the previous section and shown in Fig. 8, the regions observed are not idealized Strömgren spheres and therefore a shallower slope is expected for the luminosity–velocity dispersion relation. An un-weighted fit to the data reveals $\log(L) = (4.18 \pm 0.21) \times \log(\sigma) + (33.61 \pm 0.31)$.

We re-address the argument that the regions are virialized, given that the non-weighted fit most closely approximates $L \propto \sigma^4$ as the best description of the data. This scaling is expected from the virial theorem assuming a constant mass-to-light ratio (M/L) and constant surface brightness (Faber & Jackson 1976). However, as M/L is not constant (as shown in Fig. 5) deviations from the predicted scaling relations are expected and $L \propto \sigma^4$ is no longer an appropriate test of virialization. Furthermore, the same scaling, assuming M/L is constant, can be derived from the Jeans equations such that $M_J \propto \sigma^4/G^2\Sigma_g$.

Finally, a relationship between luminosity and velocity dispersion of galaxies and the ISM has recently been observed locally (Dib, Bell & Burkert 2006; Green et al. 2010) and at high redshift (Lehnert et al. 2009; Green et al. 2010; Genzel et al. 2011). These observations have led the authors to conclude that star formation drives the large observed line-widths. Lehnert et al. (2009) suggest that the velocity dispersion is due to mechanical energy released by the star formation in the form $\sigma = (\epsilon\Sigma_*)^{0.5}$ where ϵ is the efficiency of star formation and both σ and Σ_* can be global or local properties. The relationship between star formation surface density and velocity dispersion for the star-forming regions studied here is shown in Fig. 9 with the best linear least-squares fit of $\sigma = (100 \pm 70 \times \Sigma_*)^{0.6\ \pm 0.1}$ represented by the blue dashed line. The fit is consistent with the

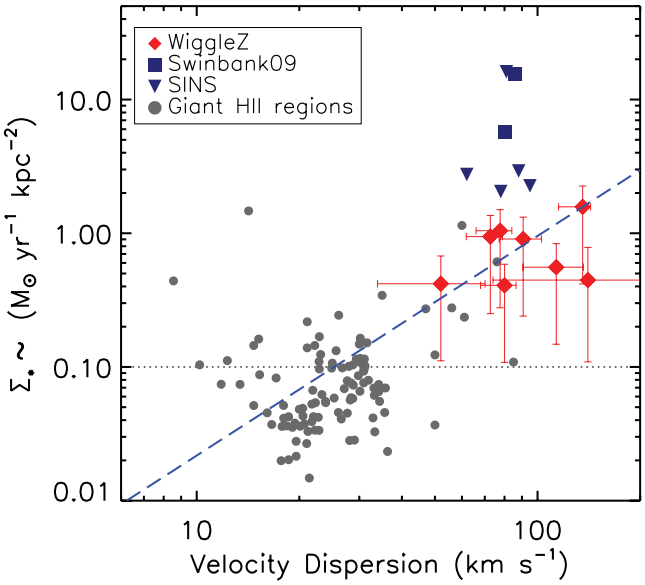

Figure 9. Star formation surface density versus velocity dispersion for the same data described in Fig. 6 with all giant H II regions shown by grey points. The blue dashed line is the least-squares best fit to the data, given by $\sigma[\mathrm{kms}^{-1}] = (100 \pm 70 \times \Sigma_*[\mathrm{M}_\odot\,\mathrm{yr}^{-1}\,\mathrm{kpc}^{-2}])^{0.6\pm0.1}$. Although this relationship is more scattered than the $L_{\mathrm{H}\alpha}$–σ relationship shown in Fig. 6 a correlation is seen, which could be a result of mechanical energy released by the star formation ($\sigma = (\epsilon\Sigma_*)^{0.5}$; Lehnert et al. 2009) or the expected star formation density in a marginally stable galactic disc of constant circular velocity assuming the KS law ($\sigma \propto \pi \mathrm{G}\Sigma_*^{0.7}/\kappa$; Krumholz & Dekel 2010). The star formation surface density is plotted for a Baldry–Glazebrook IMF.

results of Lehnert et al. (2009). However, the fit is also consistent with the expected star formation density in a marginally stable galactic disc of constant circular velocity assuming the KS law on galactic and sub-galactic scales, as noted by Krumholz & Dekel (2010). In this scenario, placing the KS law in equation (2), assuming $Q = 1$, yields $\sigma \propto \pi \mathrm{G}\Sigma_*^{0.7}/\kappa$. This interpretation is more consistent with our results in Section 5.1 and assumes the KS law holds for star-forming regions (Fig. 7). However, we note that the σ–Σ_* relation shows a much greater scatter ($R^2 = 0.57$) than the relation between luminosity and velocity dispersion ($R^2 = 0.87$).

In conclusion, we find continuous scaling relations at high and low redshift for star-forming regions between Hα size, luminosity and velocity dispersion. When the three observables are combined by comparing Hα luminosity with the Jeans mass ($M \propto \sigma^2 r_{\mathrm{cl}}/\mathrm{G}$) the scatter is significantly reduced ($L - \sigma$: $R^2 = 0.87$, $L - r$: $R^2 = 0.82$ and $L - M_J$: $R^2 = 0.9$). Some of the scatter observed in the size–velocity dispersion relation may be a natural consequence of the KS law such that $\sigma^2 \propto \Sigma_{\mathrm{g}}$. The data support the theoretical arguments that star-forming regions form out of Jeans collapse in an isothermal disc with their luminosities approximated by Strömgren spheres, with clumps accounting for 40–60 per cent of the stellar mass of the discs. These results indicate that star-forming regions at high redshift form through similar processes as star-forming regions locally.

6 CLUMP STABILITY AND SURVIVAL

It may be predicted as a consequence of the changes in global environment that star-forming regions at high redshift should not resemble star-forming regions locally. The high accretion rates predicted to drive up turbulence in the early Universe are expected to dissipate on cosmological time-scales for the most massive systems and contribute minimally at the present epoch (Dekel & Birnboim 2006). Yet despite the increased sizes and dispersions, the regions presented here ($z \sim 1.3$) have overlapping star formation surface densities and mass densities with giant H II regions in the local universe and form continuous scaling relations with local star formation regions. This indicates that while the turbulence of discs may have important implications for the size and luminosity of regions which form within them, the same processes govern their formation from high redshift to the current epoch.

Given the supersonic line-widths observed in the WiggleZ clumps and local H II regions, star formation is expected to occur rapidly, depleting the available gas for star formation within a dynamical time. For the gas to remain turbulent as is observed, a mechanism is required to stir up the ISM (Stone, Ostriker & Gammie 1998; Mac Low et al. 1998). Yet, there is no consensus in the field as to what generates gas velocity dispersions across these different epochs. The possible drivers of the turbulence at low redshift are gravitational support (Terlevich & Melnick 1981), hydrodynamical flows in the form of stellar winds (Gallagher & Hunter 1983; Arsenault & Roy 1988; Tenorio-Tagle, Munoz-Tunon & Cox 1993), champagne flows (Gallagher & Hunter 1983), supernova feedback (Mac Low & Klessen 2004; Joung, Mac Low & Bryan 2009) and bow shocks (Tenorio-Tagle et al. 1993). These general scenarios have also been put forward to account for what maintains and drives up the turbulence at high redshift as well (Immeli et al. 2004b; Bournaud et al. 2007; Förster Schreiber et al. 2006; Genzel et al. 2006; Dekel et al. 2009; Krumholz & Dekel 2010; Aumer et al. 2010; Elmegreen & Burkert 2010; Genel et al. 2010) in addition to gas accretion (Förster Schreiber et al. 2006; Genzel et al. 2006; Elmegreen & Burkert 2010; Genel et al. 2010) and star formation (Lehnert et al. 2009; Green et al. 2010). In this section, the available data and models are compared where possible to explore the implications of the previous sections in the context of clump formation and lifetimes.

Models predict that the dominant feedback mechanism at high redshift is likely radiation pressure which can drive up the turbulent motions in the ISM (Krumholz & Dekel 2010; Murray et al. 2010). Radiation feedback can provide pressure support to the clumps as well as drive large stellar winds. However, if strong enough, radiation feedback can act to disrupt the clumps before virializing and migrating to the centre to form a stellar bulge (Genel et al. 2012; Murray et al. 2010). Injection of energy into the ISM by radiation pressure could be confirmed by detecting massive radiation-driven outflows from clumps (Krumholz & Dekel 2010). In Section 3.3 an underlying broad component is detected, which contributes ∼40 per cent to the total emission-line flux from the clumps. The broad Hα component represents feedback due to thermal pressure from ionized gas and shocked stellar winds. These results, in combination with similar findings from $z \sim 2$ clumps (Genzel et al. 2011), provide evidence that winds from clumps could inject energy into the system, which would in turn drive up the turbulent motions in the ISM in accordance with the theoretical models.

If the clumps do survive feedback and clump–clump interactions then they may coalesce to form a bulge with high-velocity dispersion ∼600 Myr into the clumpy phase (Elmegreen et al. 2008). From the kinematic sample of 13 WiggleZ galaxies studied in Paper I, five galaxies show a single-resolved region of emission. Two of these galaxies show rotation, and could be interpreted as the final coalescence stage predicted by the models that include clump migration. These galaxies have average stellar masses of $3 \times 10^{10}\,\mathrm{M}_\odot$ and are still forming stars at a rate of 30 $\mathrm{M}_\odot\,\mathrm{yr}^{-1}$

with velocity dispersions of $100\,\mathrm{km\,s^{-1}}$. In the kinematic sample three galaxies exhibit multiple clumps, five are confused with extended regions of emission and five show single-resolved regions of emission. The 10 galaxies not studied in detail in this paper may also be 'clumpy' galaxies but due to projection or resolution effects individual regions are not distinguishable. However, the clumpy phase of these discs is expected to be short and thus we do not expect all galaxies observed to be in the early clumpy stage.

A different interpretation of the high-redshift data suggests that the turbulent motions arise from star formation (Lehnert et al. 2009). This analysis, based on the correlation between disc velocity dispersions and Hα luminosity, is supported locally by a study of luminous galaxies at $z \sim 0.1$ (Green et al. 2010) and in models (Elmegreen & Burkert 2010). We also find a tight scaling relation between luminosity and velocity dispersion (Fig. 6) and a noisier correlation between star formation surface density and velocity dispersion (Fig. 9). However, these two parameters may be linked by the high dispersions within a Toomre unstable disc which drive up the star formation via the KS law, such that $\sigma \propto \Sigma_*^{1.4}$ (Krumholz & Dekel 2010), as discussed in the previous section. Unfortunately, these arguments raise the problem of which is the cause and effect, high turbulence or high SFRs? We note that the mechanisms we have suggested to generate turbulence could also be interpreted as driving up star formation.

Ceverino et al. (2012) argue that because turbulent motion can dissipate over a dynamical time, ∼10 times shorter than clump lifetimes, then shortly after forming clumps must be supported against total free-fall collapse by internal rotation. Rotation also provides some support to clumps in the models of Dekel et al. (2009), Agertz et al. (2009) and Aumer et al. (2010). In simulations, clumps have rotation velocities $\sim 120\,\mathrm{km\,s^{-1}}$ and velocity dispersions comparable to disc velocity dispersions (Ceverino et al. 2012). However, in this simulation the rotational signature of clumps is found to be reduced by a factor of 7 in observations for beam-smearing of 0.1 arcsec, comparable to the data from current IFS studies. This implies that the expected observed velocity gradients of clumps, $V_{\rm rot} \sim 10 - 40\,\mathrm{km\,s^{-1}}$, are not measurable above the errors with current instrumentation. The clumps extracted from discs in these simulations have similar properties to the observed star-forming regions, as shown in the first panel of Fig. 6. The simulated and observed regions overlap in size and dispersion with a similar scatted in velocity dispersion at a given radius.

We test this model using the prescription of Ceverino et al. (2012) which requires that clumps are rotationally supported when $V_{\rm rot}^2/V_{\rm circ}^2 > 0.5$ or $V_{\rm rot}/\sigma_{\rm 1D} > \sqrt{2}$. We estimate for the WiggleZ clumps $V_{\rm rot}/\sigma_{\rm 1D}$ in which $\sigma_{\rm 1D} \sim \sigma_{\rm net}$ and $V_{\rm rot} \sim v_{\rm shear} \times 7$ (correcting for beam-smearing assuming by a factor of 7) where $v_{\rm shear}$ is the velocity shear across the clumps as measure from the average of the maximum and minimum velocity residuals within the clump radius (∼20–80 $\mathrm{km\,s^{-1}}$ for the WiggleZ clumps). Using this prescription we find that all regions could be rotationally supported. However, these conclusions are uncertain given our measurement errors. Observed clumps at $z \sim 2$ show tentative evidence for rotational support for a fraction of the sample, with velocity shear measured from residual Hα velocity maps after model discs have been subtracted (Genzel et al. 2011). Together, these results suggest rotation is not likely to be the primary support mechanism for the observed clumps. If clumps survive long enough to virialize then they could become rotationally supported. A more suitable test would be to observe the kinematics of more evolved clumps, seen in broad-band imaging, which may have had time to virialize.

In conclusion, there are many processes internal and external to galaxies that are able to inject energy into the ISM to maintain the high observed velocity dispersions. The WiggleZ clumps have consistent low metallicity across the discs they are embedded in, indicating that they are young with common evolution histories. They do not show evidence of rotation suggesting that they have not virialized. However, this interpretation is limited by our data due to the effects of beam-smearing. Higher S/N and higher resolution data of many more clumps are needed to provide more rigorous tests of the existing theories of clump evolution at high redshift.

7 CONCLUSIONS

We present eight new clumps embedded within unstable disc galaxies at $z \sim 1.3$ from the kinematic sub-sample of the WiggleZ Dark Energy Survey (Paper I). The clumps have the following properties:

(i) Average clump size of $r_{\rm core} \sim 1.5$ kpc.

(ii) Average clump velocity dispersions of $\sigma \sim 90\,\mathrm{km\,s^{-1}}$, higher than all other clump samples at $z > 1$.

(iii) Average Jeans masses of $8.4 \times 10^9\,\mathrm{M_\odot}$, in total accounting for 40–60 per cent of the stellar mass of the discs.

(iv) Estimated gas mass surface densities in the range $\Sigma_{\rm g} =$ 300–2000 $\mathrm{M_\odot\,pc^{-2}}$.

(v) Clump star formation surface densities of $\Sigma_* = 0.4$–2 $\mathrm{M_\odot\,yr^{-1}\,kpc^{-2}}$, with total clump star formation accounting for 30–40 per cent of star formation in the discs (BG03 IMF).

(vi) In the stacked spectrum of all clumps we detect a broad Hα component of FWHM $\sim 490\,\mathrm{km\,s^{-1}}$ which contributes 40 per cent to the overall clump flux and is likely due to the presence of large-scale stellar winds driven by intense star formation. This conclusion is supported by the condition that all clumps are above the threshold required to drive galactic scale winds, $\Sigma_* > 0.1\,\mathrm{M_\odot\,yr^{-1}\,kpc^{-2}}$.

Clumps, H II regions and giant H II regions are found to follow the same scaling relations for Hα size, velocity dispersion and luminosity, indicating that they may be scaled-up versions of local H II regions. Our best-fitting relations are $\log(\sigma) = (0.42 \pm 0.03) \times \log(d) + (0.33 \pm 0.09)$, $\log(L_{\rm H\alpha}) = (2.72 \pm 0.04) \times \log(d) + (31.99 \pm 0.08)$ and $\log(L_{\rm H\alpha}) = (4.18 \pm 0.21) \times \log(\sigma) + (33.61 \pm 0.31)$. We show that these relationships hold over four orders of magnitude in mass ($10^6 - 10^{10}\,\mathrm{M_\odot}$) from H II regions to giant clumps at high redshift. The size–velocity dispersion relation is consistent with Jeans collapse in an isothermal disc with a range in star formation surface density of $\sim 4000\,\mathrm{M_\odot\,pc^{-2}}$. The regions closely approximate the expected relation for idealized Strömgren spheres although they may not be completely ionization bound as a slightly shallower relation is observed. This could be due to a range of factors including resolution, cloud density, dust, metallicity and magnetic fields.

The relationship between luminosity and velocity dispersion is not as well understood. We find an empirical relation of $L \propto \sigma^4$, which deviates from the predicted relation $L \propto \sigma^6$ assuming that star-forming regions form under Jeans collapse and their luminosities are driven by the Strömgren sphere physics. A possible explanation for the empirical relation is that the luminosity closely traces the mass, such that $M \propto \sigma^4/\mathrm{G}^2\Sigma$, a scaling obtained for both the Jeans and virial masses. We find that the Jeans mass yields a mass in better agreement with models than the dynamical mass and thus is the more likely driver of the observed correlation.

The data are consistent with high surface densities as a result of higher velocity dispersions in a marginally unstable disc assuming a KS law (Krumholz & Dekel 2010). This is a reasonable

approximation given that we find tentative evidence that star-forming regions follow the KS law. If this star formation law holds then an expected range in the gas surface density would explain the high scatter in the σ–r relation and would predict gas surface densities in agreement with estimates from the Jeans equations.

We do not find a luminosity offset between our clumps and local H II regions as reported for other high-redshift studies (Swinbank et al. 2009; Jones et al. 2010). We extract measurements from the literature for giant H II regions in isolated spirals, (U) LIRGs, irregulars and dwarf irregulars. After correcting historical data for updated distances and cosmologies we find that H II regions and giant H II regions follow a single size–luminosity relationship. A few outliers persist locally from the LIRG merger of NGC 4038 and NGC 4039 (Bastian et al. 2006) and sub-L_* galaxies at $z \sim 2$ (Jones et al. 2010) and an L_* galaxy at $z \sim 5$ (Swinbank et al. 2009). This offset could be due to a difference in how regions are measured, as both high-redshift studies used the isophote method rather than profile fitting and the determination of sizes in the low-redshift sample is unclear.

We determine that the most consistent method to measure the size of an H II region is from its core radius determined by fitting a Gaussian profile to the central brightest region of Hα emission. Theoretically, this measurement is based on the formation of idealized fully ionized regions that are not contaminated along the line of sight with intervening gas and dust. Observationally, this measurement is insensitive to variations in the background; however it becomes difficult to measure in low S/N data.

The results presented here are in relative agreement with massive star-forming regions forming out of Toomre-unstable discs with high local velocity dispersion, with measured sizes and estimated masses in agreement with the model predictions (e.g. Noguchi 1999; Immeli et al. 2004a,b; Bournaud et al. 2007; Elmegreen et al. 2008). The data support models that employ radiation feedback in the form of large stellar winds driven by regions of enhanced star formation (Krumholz & Dekel 2010; Genel et al. 2012); however we cannot say on what time-scale the winds would destroy the clumps. The dominant mechanism stabilizing clumps from rapid collapse is unclear. Given the importance of high-velocity dispersions in the formation of large massive star-forming regions and minimal signature of rotation, turbulence is likely an important contributor. For the discs to become initially unstable the injection of energy from cold accretion is the probable cause. However, different mechanisms may dominate throughout the lifetime of the discs, such as disc instabilities and feedback from young stars, both of which are observed here (Elmegreen & Burkert 2010). There are many possible mechanisms that may produce local velocity dispersions – inflow, winds, shocks, gravitational energy, star formation – further research is needed to understand the interplay of their significance throughout the lifetimes of high-redshift discs.

ACKNOWLEDGMENTS

We thank the referee for providing valuable comments. EW thanks Max Malacari and Nadine Bachmann for their valuable help on measuring clump sizes and Mark Swinbank and Rachel Livermore for useful discussions.

Some of the data presented herein were obtained at the W.M. Keck Observatory, which is operated as a scientific partnership among the California Institute of Technology, the University of California and the National Aeronautics and Space Administration. The Observatory was made possible by the generous financial support of the W.M. Keck Foundation. The authors wish to recognize and acknowledge the very significant cultural role and reverence that the summit of Mauna Kea has always had within the indigenous Hawaiian community. We are most fortunate to have the opportunity to conduct observations from this mountain.

REFERENCES

Agertz O., Teyssier R., Moore B., 2009, MNRAS, 397, L64
Alexander D. M., Swinbank A. M., Smail I., McDermid R., Nesvadba N. P. H., 2010, MNRAS, 402, 2211
Arsenault R., Roy J., 1988, A&A, 201, 199
Aumer M., Burkert A., Johansson P. H., Genzel R., 2010, ApJ, 719, 1230
Baldry I. K., Glazebrook K., 2003, ApJ, 593, 258 (BG03)
Bastian N., Emsellem E., Kissler-Patig M., Maraston C., 2006, A&A, 445, 471
Beckman J. E., Rozas M., Zurita A., Watson R. A., Knapen J. H., 2000, AJ, 119, 2728
Binney J., Tremaine S., 2008, in Binney J., Tremaine S., eds, Galactic Dynamics, 2nd edn. Princeton Univ. Press, Princeton
Blitz L., Fukui Y., Kawamura A., Leroy A., Mizuno N., Rosolowsky E., 2007, in Reipurth B., Jewitt D., Keil K., eds, Protostars and Planets V, Univ. Arizona Press, Tucson, p. 81
Bolatto A. D., Leroy A. K., Rosolowsky E., Walter F., Blitz L., 2008, ApJ, 686, 948
Bournaud F., Elmegreen B. G., Elmegreen D. M., 2007, ApJ, 670, 237
Bournaud F. et al., 2008, A&A, 486, 741
Burkert A. et al., 2010, ApJ, 725, 2324
Ceverino D., Dekel A., Bournaud F., 2010, MNRAS, 404, 2151
Ceverino D., Dekel A., Mandelker N., Bournaud F., Burkert A., Genzel R., Primack J., 2012, MNRAS, 420, 3490
Combes F., García-Burillo S., Braine J., Schinnerer E., Walter F., Colina L., 2011, A&A, 528, A124
Cowie L. L., Hu E. M., Songaila A., 1995, AJ, 110, 1576
Daddi E. et al., 2010, ApJ, 713, 686
Davies R. et al., 2011, ApJ, 741, 69
Dekel A., Birnboim Y., 2006, MNRAS, 368, 2
Dekel A., Birnboim Y., 2008, MNRAS, 383, 119
Dekel A., Sari R., Ceverino D., 2009, ApJ, 703, 785
Dib S., Bell E., Burkert A., 2006, ApJ, 638, 797
Dickinson M., 2001, in Hammer F. et al., eds, Building Galaxies: From the Primordial Universe to the Present, Moriond Astrophysics Meeting (1999 March), Editions Frontieres, Paris, p. 257
Drinkwater M. J. et al., 2010, MNRAS, 401, 1429
Elmegreen B. G., 1989, ApJ, 338, 178
Elmegreen B. G., Burkert A., 2010, ApJ, 712, 294
Elmegreen B. G., Elmegreen D. M., 2005, ApJ, 627, 632
Elmegreen B. G., Bournaud F., Elmegreen D. M., 2008, ApJ, 688, 67
Elmegreen D. M., Elmegreen B. G., Marcus M. T., Shahinyan K., Yau A., Petersen M., 2009, ApJ, 701, 306
Faber S. M., Jackson R. E., 1976, ApJ, 204, 668
Ferguson A. M. N., Wyse R. F. G., Gallagher J. S., III, Hunter D. A., 1996, AJ, 111, 2265
Förster Schreiber N. M. et al., 2006, ApJ, 645, 1062
Förster Schreiber N. M. et al., 2009, ApJ, 706, 1364
Förster Schreiber N. M., Shapley A. E., Erb D. K., Genzel R., Steidel C. C., Bouché N., Cresci G., Davies R., 2011a, ApJ, 731, 65
Förster Schreiber N. M. et al., 2011b, ApJ, 739, 45
Fuentes-Masip O., Muñoz-Tuñón C., Castañeda H. O., Tenorio-Tagle G., 2000, AJ, 120, 752
Gallagher J. S., Hunter D. A., 1983, ApJ, 274, 141
Genel S., Bouché N., Naab T., Sternberg A., Genzel R., 2010, ApJ, 719, 229
Genel S. et al., 2012, ApJ, 745, 11
Genzel R. et al., 2006, Nat, 442, 786
Genzel R. et al., 2011, ApJ, 733, 101
Green A. W. et al., 2010, Nat, 467, 684

Guo Y., Giavalisco M., Ferguson H. C., Cassata P., Koekemoer A. M., 2011, preprint (arXiv e-prints)
Gutiérrez L., Beckman J. E., Buenrostro V., 2011, AJ, 141, 113
Heckman T. M., Armus L., Miley G. K., 1990, ApJS, 74, 833
Heckman T. M., Lehnert M. D., Strickland D. K., Armus L., 2000, ApJS, 129, 493
Heyer M., Krawczyk C., Duval J., Jackson J. M., 2009, ApJ, 699, 1092
Immeli A., Samland M., Gerhard O., Westera P., 2004a, A&A, 413, 547
Immeli A., Samland M., Westera P., Gerhard O., 2004b, ApJ, 611, 20
Jones T. A., Swinbank A. M., Ellis R. S., Richard J., Stark D. P., 2010, MNRAS, 404, 1247
Joung M. K. R., Mac Low M.-M., 2006, ApJ, 653, 1266
Joung M. R., Mac Low M.-M., Bryan G. L., 2009, ApJ, 704, 137
Kennicutt R. C., Jr, 1979, ApJ, 228, 696
Kennicutt R. C., Jr, 1998, ARA&A, 36, 189
Kennicutt R. C., Jr et al., 2003, PASP, 115, 928
Kennicutt R. C., Jr et al., 2007, ApJ, 671, 333
Krumholz M. R., Dekel A., 2010, MNRAS, 406, 112
Larkin J. et al., 2006, New Astron. Rev., 50, 362
Larson R. B., 1981, MNRAS, 194, 809
Law D. R., Steidel C. C., Erb D. K., Larkin J. E., Pettini M., Shapley A. E., Wright S. A., 2007, ApJ, 669, 929
Le Tiran L., Lehnert M. D., Di Matteo P., Nesvadba N. P. H., van Driel W., 2011a, A&A, 530, L6
Lehnert M. D., Nesvadba N. P. H., Tiran L. L., Di Matteo P., van Driel W., Douglas L. S., Chemin L., Bournaud F., 2009, ApJ, 699, 1660
Le Tiran L., Lehnert M. D., van Driel W., Nesvadba N. P. H., Di Matteo P., 2011b, A&A, 534, L4
Mac Low M.-M., Klessen R. S., 2004, Rev. Modern Phys., 76, 125
Mac Low M.-M., Klessen R. S., Burkert A., Smith M. D., 1998, Phys. Rev. Lett., 80, 2754
McCall M. L., Hill R., English J., 1990, AJ, 100, 193
Melnick J., Moles M., Terlevich R., Garcia-Pelayo J.-M., 1987, MNRAS, 226, 849
Monreal Ibero A., Colina L., Arribas S., García-Marín M., 2007, A&A, 472, 421
Murray N., Quataert E., Thompson T. A., 2010, ApJ, 709, 191
Noguchi M., 1999, ApJ, 514, 77
Osterbrock D. E., 1989, Astrophysics of Gaseous Nebulae and Active Galactic Nuclei, Univ. Science Books, Mill Valley
Pettini M., Pagel B. E. J., 2004, MNRAS, 348, L59
Pleuss P. O., Heller C. H., Fricke K. J., 2000, A&A, 361, 913
Relaño M., Beckman J. E., Zurita A., Rozas M., Giammanco C., 2005, A&A, 431, 235
Rozas M., Richer M. G., López J. A., Relaño M., Beckman J. E., 2006, A&A, 455, 539
Sandage A., Tammann G. A., 1974, ApJ, 190, 525
Schmidt M., 1959, ApJ, 129, 243
Shapiro K. L. et al., 2009, ApJ, 701, 955
Smith M. G., Weedman D. W., 1970, ApJ, 161, 33
Solomon P. M., Rivolo A. R., Barrett J., Yahil A., 1987, ApJ, 319, 730
Spitzer L., Jr, 1942, ApJ, 95, 329
Stone J. M., Ostriker E. C., Gammie C. F., 1998, ApJ, 508, L99
Swinbank A. M. et al., 2009, MNRAS, 400, 1121
Swinbank A. M. et al., 2010, Nat, 464, 733
Tacconi L. J. et al., 2010, Nat, 463, 781
Tenorio-Tagle G., Munoz-Tunon C., Cox D. P., 1993, ApJ, 418, 767
Terlevich R., Melnick J., 1981, MNRAS, 195, 839
Toomre A., 1964, ApJ, 139, 1217
Tully R. B., Rizzi L., Shaya E. J., Courtois H. M., Makarov D. I., Jacobs B. A., 2009, AJ, 138, 323
van Dam M. A. et al., 2006, PASP, 118, 310
van den Bergh S., Abraham R. G., Ellis R. S., Tanvir N. R., Santiago B. X., Glazebrook K. G., 1996, AJ, 112, 359
van Starkenburg L., van der Werf P. P., Franx M., Labbé I., Rudnick G., Wuyts S., 2008, A&A, 488, 99
Wisnioski E. et al., 2011, MNRAS, 417, 2601 (Paper I)
Wizinowich P. L. et al., 2006, PASP, 118, 297

APPENDIX A: CORRECTIONS TO CLUMP AND H II REGION MEASUREMENTS

This appendix summarizes the methods employed to calculate sizes, luminosities and velocity dispersions from the literature, used for comparison with WiggleZ clumps. Details of the corrections we introduced to improve the accuracy of comparison are included.

A1 H II Regions

SINGS measurements

From the SINGS survey we measure H II region size and luminosities from NGC 24, NGC 628, NGC 925, NGC 1566, NGC 4254, NGC 3938, NGC 7552 as detailed in Section 3. These galaxies were chosen for the availability of high-quality Hα images and high numbers of H II regions.

A2 Giant H II regions

Gallagher & Hunter (1983)

The Hα flux is measured within a fixed 200 pc radius for each H II region. This essentially yields the flux within the core radius. The authors estimate that there is up to a factor of 2 error in the flux measurements. Velocity dispersions are corrected for Doppler broadening and instrumental broadening. We recalculate the luminosity and diameters with $H_0 = 70\,\mathrm{km\,s^{-1}\,Mpc^{-1}}$ from $H_0 = 50\,\mathrm{km\,s^{-1}\,Mpc^{-1}}$ originally used in the paper, using new distances from the EDD.

Arsenault & Roy (1988)

Recalculation of H II region luminosities and diameters with $H_0 = 70\,\mathrm{km\,s^{-1}\,Mpc^{-1}}$ and new distances from the EDD is readily possible as the authors provide the original measurements of angular diameter and Hα flux. Velocity dispersions are not measured for this sample.

Bastian et al. (2006)

Six H II regions are observed in the Antennas galaxies, NGC 4038 and NGC 4039, with the Very Large Telescope – Visible Multi-Object Spectrograph (VLT-VIMOS) IFS. The Hγ, Hβ and [O III] emission lines are observed. The Antennas is classified as an LIRG. Luminosities are inferred from Hβ and converted to Hα assuming case B recombination (10 000 K). We recalculate the luminosity and diameters with $H_0 = 70\,\mathrm{km\,s^{-1}\,Mpc^{-1}}$ from $H_0 = 75\,\mathrm{km\,s^{-1}\,Mpc^{-1}}$ originally used in the paper, with a new distance of $D = 19.2$ Mpc from the EDD.

Rozas et al. (2006)

This sample includes only the intrinsically brightest H II regions within NGC 157, NGC 925, NGC 3631, NGC 6764, NGC 3344, NGC 4321, NGC 5364, NGC 5055, NGC 5985 and NGC 7479. The purpose of the selection was to choose the youngest, most massive normal star clusters to minimize the processes available to drive the H II region away from virial equilibrium. To find an accurate velocity dispersion the authors determine the optimal number of Gaussian components to fit to each line profile using the component which contributes the most luminosity in each H II region. For region size they adopt one half the total radius given in H II region catalogues as specified by Relaño et al. (2005), which is based on the 40 per cent isophote method of McCall, Hill & English (1990),

which is equivalent to our core method. The velocity dispersion is measured within this radius and was corrected for natural broadening, Doppler broadening and instrumental broadening. We recalculate the luminosity and diameters with $H_0 = 70\,\mathrm{km\,s^{-1}\,Mpc^{-1}}$ from $H_0 = 75\,\mathrm{km\,s^{-1}\,Mpc^{-1}}$ originally used in the paper, with new distances from the EDD.

Monreal-Ibero et al. (2007)

The regions selected from this paper are tidal dwarf galaxy candidates. However, they are selected in a similar manner to other high- and low-redshift regions used for comparison in this paper and as such we include them as giant H II regions. They are selected within five local ULIRGs with the Wide-Field Planetary Camera 2 (WFPC2) and IFS data. Isophotal and effective radii are measured for all regions. We use the effective radii as it better approximates the core method. Luminosity is recalculated from the given flux values without extinction correction.

A3 High-redshift clumps

SINS survey: Genzel et al. (2011) and Förster Schreiber et al. (2011b)

The clump data taken from Genzel et al. (2011) are for BX482-clumpA, ZC782941-clumpA, ZC406690-clumpA, ZC406690-clumpB and ZC406690-clumpC. Integrated clump properties such as BX599-all and D3a15504-clumpsA-F are excluded. Clump radii are given by the half width half maximum (HWHM) from Gaussian fits to clumps in velocity channels of the IFS data cube. The instrumental resolution is subtracted in quadrature. We convert the HWHM to the rms of a Gaussian profile, the radius used for the core method, by $r_{\mathrm{core}} = \frac{2\mathrm{HWHM}}{\sqrt{2\log 2}}$. The velocity dispersion of the clumps is the intrinsic local velocity dispersion after removal of beam-smeared rotation and instrumental resolution.

The clump data taken from Förster Schreiber et al. (2011b) are exclusively from BX482. Clump-1 in this sample is defined to be the same clump as BX482-clumpA in Genzel et al. (2011). In Förster Schreiber et al. (2011b) the flux, $F_{\mathrm{obs}} = 3.92 \pm 0.05 \times 10^{-17}$ erg $\mathrm{s^{-1}\,cm^{-2}}$ is measured within $r_{\mathrm{phot}} = 2.3\,\mathrm{kpc}$ and has $R_{\mathrm{HWHM}} = 0.96\,\mathrm{kpc}$ in Genzel et al. (2011) the $R_{\mathrm{HWHM}} = 1\,\mathrm{kpc}$ and $F_{\mathrm{obs}} = 3.5 \times 10^{-17}$ erg $\mathrm{s^{-1}\,cm^{-2}}$. For comparison purposes we use r_{phot} radii.

Swinbank et al. (2009) and Jones et al. (2010)

Swinbank et al. (2009) and Jones et al. (2010) publish clumps in L_* lensed galaxies at $z \sim 2$–4 from IFS data. They derive sizes using the isophote method. We correct the cosmology to $H_0 = 70\,\mathrm{km\,s^{-1}\,Mpc^{-1}}$ and $\Omega_{\mathrm{M}} = 0.27$, $\Omega_{\Lambda} = 0.73$.

This paper has been typeset from a TEX/LATEX file prepared by the author.